Systems/Circuits

Organization of Cortical and Thalamic Input to Inhibitory Neurons in Mouse Motor Cortex

Sandra U. Okoro,[1] Roman U. Goz,[1] Brigdet W. Njeri,[1] Madhumita Harish,[1] Catherine F. Ruff,[1] Sarah E. Ross,[1] Charles Gerfen,[2] and Bryan M. Hooks[1]

[1]University of Pittsburgh School of Medicine, Pittsburgh, Pennsylvania 15261, and [2]National Institute of Mental Health, Bethesda, Maryland 20892

Intracortical inhibition in motor cortex (M1) regulates movement and motor learning. If cortical and thalamic inputs target different inhibitory cell types in different layers, then these afferents may play different roles in regulating M1 output. Using mice of both sexes, we quantified input to two main classes of M1 interneurons, parvalbumin+ (PV+) cells and somatostatin+ (SOM+) cells, using monosynaptic rabies tracing. We then compared anatomic and functional connectivity based on synaptic strength from sensory cortex and thalamus. Functionally, each input innervated M1 interneurons with a unique laminar profile. Different interneuron types were excited in a distinct, complementary manner, suggesting feedforward inhibition proceeds selectively via distinct circuits. Specifically, somatosensory cortex (S1) inputs primarily targeted PV+ neurons in upper layers (L2/3) but SOM+ neurons in middle layers (L5). Somatosensory thalamus [posterior nucleus (PO)] inputs targeted PV+ neurons in middle layers (L5). In contrast to sensory cortical areas, thalamic input to SOM+ neurons was equivalent to that of PV+ neurons. Thus, long-range excitatory inputs target inhibitory neurons in an area and a cell type-specific manner, which contrasts with input to neighboring pyramidal cells. In contrast to feedforward inhibition providing generic inhibitory tone in cortex, circuits are selectively organized to recruit inhibition matched to incoming excitatory circuits.

Key words: **circuit mapping; interneurons; motor cortex; parvalbumin; rabies tracing; somatostatin**

Significance Statement

M1 integrates sensory information and frontal cortical inputs to plan and control movements. Although inputs to excitatory cells are described, the synaptic circuits by which these inputs drive specific types of M1 interneurons are unknown. Anatomical results with rabies tracing and physiological quantification of synaptic strength shows that two main classes of inhibitory cells (PV+ and SOM+ interneurons) both receive substantial cortical and thalamic input, in contrast to interneurons in sensory areas (where thalamic input strongly prefers PV+ interneurons). Further, each input studied targets PV+ and SOM+ interneurons in a different fashion, suggesting that separate, specific circuits exist for recruitment of feedforward inhibition.

Introduction

Rodent motor cortex (M1; Donoghue and Wise, 1982; Porter and White, 1983) integrates input from sensory cortex (S1) and thalamus to plan and control movement. Excitatory connectivity to pyramidal neurons has been studied, but how different interneuron types are recruited by long-range input has received less attention. Cortical and thalamic sensory inputs arrive in M1, resulting in sensory-related activity (Ferezou et al., 2007; Hatsopoulos and Suminski, 2011; Murray and Keller, 2011; Huber et al., 2012), consistent with a role for M1 in active sensation (Hill et al., 2011) and sensorimotor learning (Asanuma, 1981). S1 input (Hoffer et al., 2003) excites pyramidal neurons primarily in upper M1 layers (Porter et al., 1990; Kaneko et al., 1994a; Mao et al., 2011). Somatosensory input to M1 also originates from higher-order sensory thalamus, including posterior nucleus (PO; Deschênes et al., 1998; Ohno et al., 2012; Harris et al., 2019). These classes of input (S1 and PO) both strongly excited pyramidal neurons of L2/3 and L5A (Mao et al., 2011; Hooks et al., 2013; Hooks, 2017). L2/3 and L5A neurons then provide descending input to L5B pyramidal neurons that regulate movement

Received May 18, 2022; revised Sep. 1, 2022; accepted Sep. 6, 2022.

Author contributions: C.G. and B.M.H. designed research; S.U.O., R.U.G., B.W.N., C.F.R., C.G., and B.M.H. performed research; M.H., C.F.R., S.E.R., and C.G. contributed unpublished reagents/analytic tools; R.U.G., M.H., C.G., and B.M.H. analyzed data; B.M.H. wrote the paper.

This work was supported by a NARSAD Young Investigator Award (B.M.H.), National Institutes of Health–National Institute of Neurological Disorders and Stroke Grant R01 NS103993 (B.M.H.), and Congressionally Directed Medical Research Program–Peer Reviewed Medical Research Program Discovery Award PR201842 (R.U.G. and B.M.H.) and a National Institute of Mental Health IRP award (ZIA MH002497-33) to C.G. We thank Caroline Runyan, Chinfei Chen, Nuo Li, Srivatsun Sadagopan, Taehyeon Kim, Shelby Ruiz, and other members of the Hooks lab for comments and suggestions, and Jay Couey, who performed whole-cell recordings contributing to the circuit mapping and short-term plasticity experiments.

The authors declare no competing financial interests.

Correspondence should be addressed to Bryan M. Hooks at hooksm@pitt.edu.

https://doi.org/10.1523/JNEUROSCI.0950-22.2022

(Kaneko et al., 1994b; Weiler et al., 2008; Anderson et al., 2010; Hooks et al., 2011; Kiritani et al., 2012).

A diverse range of cortical GABAergic interneuron types play an important role in regulating cortical excitation (Tremblay et al., 2016). Three major classes include parvalbumin-expressing (PV+), somatostatin-expressing (SOM+), and 5-HT3a-receptor-expressing (5HT3aR+) interneurons (Lee et al., 2010). Different interneurons connect in local circuits in distinct ways (Porter et al., 2000). PV+ and SOM+ cells are found across the width of M1 from L2 to L6 (Fig. 1; Lee et al., 2010), whereas 5-HT3aR+ cells are mostly present in the upper layers of cortex. PV+ interneurons include fast-spiking interneurons, which target perisomatic regions of pyramidal neurons. SOM+ interneurons include low-threshold spiking interneurons among a heterogeneous range of SOM+ cell types (Cauli et al., 1997; Kawaguchi and Kubota, 1997; Gibson et al., 1999; Kubota, 2014). One SOM+ interneuron subset, Martinotti cells, targets apical dendrites of pyramidal cells (Wang et al., 2004). Differences in subcellular targeting of excitatory cells contributes to different roles in regulating cortical output. Thus, understanding how different classes of interneuron are activated by distinct excitatory inputs is an important step in understanding how feedforward inhibition is recruited by different cortical afferents.

We tested whether the connectivity of long-range inputs to PV+ and SOM+ interneurons in M1 follows the pattern from sensory cortex studies. Because ascending thalamic inputs in sensory cortical areas principally target PV+ interneurons, we hypothesized that M1 PV+ interneurons would similarly be the major recipients of thalamic input. These conclusions are derived from studies of the connectivity of principal thalamic nuclei to cortical layer 4 (White, 1979; Keller and White, 1987; Hirsch et al., 2003; Cruikshank et al., 2007, 2010), which is absent in M1. We quantified the overall pattern of input to specific interneuron types using monosynaptic rabies tracing. Because this method is not layer specific and does not directly measure synapse strength, we measured monosynaptic excitation to M1 interneurons functionally using channelrhodopsin-2 (ChR2)-assisted circuit mapping (Petreanu et al., 2007, 2009; Cruikshank et al., 2010). This assessed synaptic input strength as a function of laminar depth and specific interneuron type across layers in M1. In contrast to the strong preference of thalamocortical input for PV+ interneurons in layer 4 of sensory cortex (Cruikshank et al., 2007, 2010); both methods found thalamic input to SOM+ neurons that was nearly as strong as PV+ neuron input. The laminar pattern, however, differed. Corticocortical afferents from S1 also targeted interneurons differently across cell types; among PV+ neurons, L2/3 cells were most strongly excited, whereas for SOM+ neurons, input arrived strongly in middle layers (L5). Furthermore, comparing inputs from S1 and thalamus, PV+ neurons were targeted in a complementary fashion, with S1 exciting upper layers (L2/3) and thalamus targeting middle layers (L5). Because S1 and PO targeted excitatory neurons in similar layers (Hooks et al., 2013), the complementary pattern of input to PV+ neurons suggests that feedforward inhibition does not simply silence cortex but integrates into local circuits in a specific fashion.

Materials and Methods

Stereotactic injections

Animal protocols were approved by the Institutional Animal Care and Use Committees at the University of Pittsburgh. Mice of either sex were used. Experimental procedures were similar to those of previous studies (Hooks et al., 2013). Injections were made with glass pipettes (Drummond) using a custom-made positive displacement system (Narashige). Stereotactic coordinates are listed in Table 1. A pair of injections (50–100 nl; 500 and 800 mm depth from pia) was made in the cortex. One location (50–100 nl) was injected into thalamic targets. Cre driver mouse lines (PV-Cre, SOM-Cre, and NK1R-CreER) were used in conjunction with the lsl-tdTomato reporter line, Ai14, to label specific interneuron populations (see Table 2). Tacr1 experiments using NK1R-CreER required tamoxifen injections to drive recombination. Animals were anesthetized using isoflurane and placed in a custom stereotactic apparatus. Juvenile mice at postnatal day (P)12–P22 were injected with adeno-associated virus (AAV) expressing excitatory opsins. AAVs included CAG-ChR2-mVenus and hSyn-Chronos-GFP. AAV-CaMKIIa-hChR2(H134R)-EYFP was used in Tacr1 mapping experiments (see Table 3).

Monosynaptic viral tracing

We used AAV injections to express DIO-TVA-EGFP-B19G in potential starter cells in cerebral cortex of PV-Cre and SOM-Cre driver mouse lines (Wickersham et al., 2007b; Atasoy et al., 2008). After 2 weeks of expression time, we injected EnvA pseudotyped rabies (CVS-N2c$^{\Delta G}$ strain) into cortex and allowed 8–9 d for transport and expression (Reardon et al., 2016). Following transcardial perfusion, whole brains were sectioned, immunoamplified for EGFP and TdTomato, and stained with NeuroTrace Blue (Thermo Fisher Scientific) as a structural marker. The brain was imaged and reconstructed using NeuroInfo software (MBF Bioscience) as previously described (Hooks et al., 2018; Eastwood et al., 2019). Primary antibodies used were rabbit anti-RFP (catalog #600-401-379, Rockland) and chicken anti-GFP (catalog #A10262, Invitrogen). Secondary antibodies used were goat anti-rabbit-Alexa 555 (catalog #A32732, Invitrogen) and goat anti-chicken Alexa Fluor 488 (catalog #A32931, Invitrogen). Original images are posted at http://gerfenc.biolucida.net/link?l=Jl1tV7 (Biolucida Cloud Viewer, free download) and http://gerfenc.biolucida.net/images/?page=images&selectionType=collection&selectionId=32 (Web based). Images were aligned to the Allen Common Coordinate Framework (CCF) V3.0 (Oh et al., 2014; Kuan et al., 2015) using NeuroInfo software (MBF Bioscience). Somata were detected by NeuroInfo using an artificial neural network. Their coordinates in the Allen CCF were used to quantify in which structure the neuron was detected using custom MATLAB software. Presynaptic labeled (tdTomato+) neurons in each structure were quantified as a fraction of total labeled neurons in that brain to normalized for differences between mice and injections. For comparisons between starter cell types (PV+ or Cre+) or injection sites [frontal cortex (M2), forelimb motor cortex (fM1), somatosensory cortex (vS1)], *t* tests were performed. To reduce the number of comparisons to a manageable size, brain regions were only included in the analysis if the fraction of presynaptic neurons labeled exceeded a threshold value of 2% for 24 large brain areas (Figs. 1*O*, 2*B–D*) or 0.5% for 33 smaller thalamic nuclei (Figs. 1*P*, 2*C*,*E–H*). The two-stage procedure of Benjamini et al. (2009) was used to control the false discovery rate (FDR). Black asterisks (with *p* values noted) mark significant differences between presynaptic labeling. Gray asterisks used for comparisons not significant after correcting for FDR.

Experimental design and statistical analyses

Electrophysiology and photostimulation. Brain slices were prepared >14 d after viral infection in young adult mice (~P30–P60). Mice were anesthetized with isoflurane, and the brain was rapidly removed and placed in cooled choline-based cutting solution containing the following (in mM): 110 choline chloride, 3.1 sodium pyruvate, 11.6 sodium ascorbate, 25 $NaHCO_3$, 25 D-glucose, 7 $MgCl_2$, 2.5 KCl, and 1.25 NaH_2PO_4, 0.5 $CaCl_2$. Off-coronal sections (300 μm) of M1 were cut using a vibratome (VT1200S, Leica). Additional sections were cut to confirm injection location. Slices were incubated at 37°C in oxygenated ACSF containing the following (in mM): 127 NaCl, 25 $NaHCO_3$, 25 D-glucose, 2.5 KCl, 2 $CaCl_2$, 1 $MgCl_2$, and 1.25 NaH_2PO_4, for >30 min and maintained at room temperature (22°C) thereafter.

Whole-cell recordings were performed at 22°C in oxygenated ACSF with borosilicate pipettes (3–6 MΩ; Warner Instruments) containing

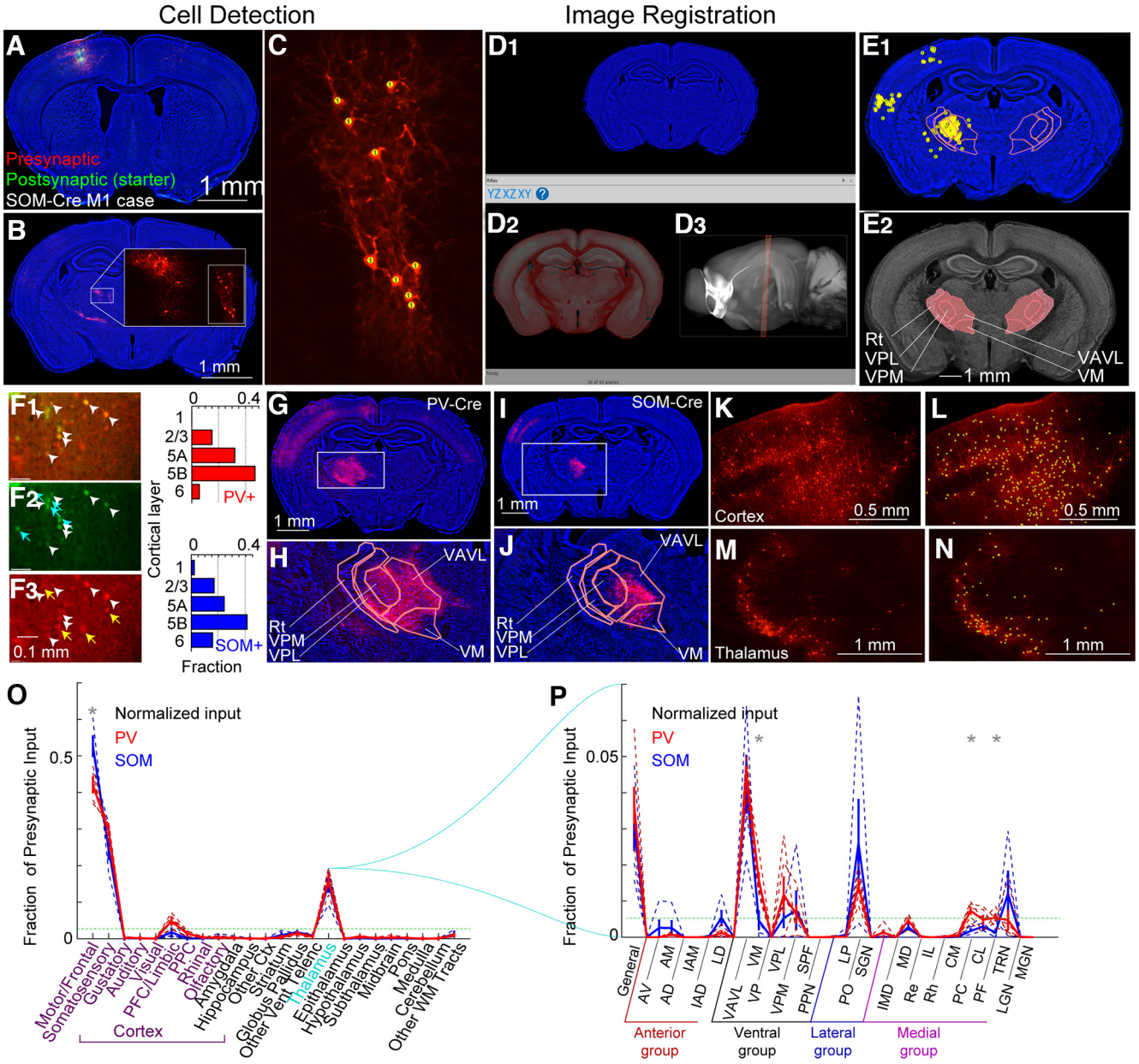

Figure 1. Monosynaptic retrograde tracing of inputs to motor cortex PV+ and SOM+ neurons. ***A***, Injection site in M1 of a SOM-Cre mouse injected with AAV-DIO-TVA-RG-EGFP (green) and EnvA pseudotyped N2c RABV-tdTomato (red). Neurotrace Blue labels the tissue structure. ***B***, Inset, tdTomato-labeled thalamic neurons. ***C***, tdTomato+ (red) somata detected in NeuroInfo. Markers are yellow. ***D1–D3***, Section registration in NeuroInfo. ***D1***, NeuroTrace Blue used as a structural marker in imaged sections. ***D2***, ***D3***, Current reference section (teal, ***D2***) and brain (black and white, ***D3***) showing the reference atlas. The reference section (***D2***) can be aligned to the current section (***D1***; overlaid in red in ***D2***) by adjusting the scale or shifting and rotating the plane in which the reference brain is sectioned (***D3***, control). The current plane orientation for the reference brain is shown as the red box in ***D3*** (slightly offset from coronal). A nonlinear transform for each section is used to register each object in the current image to the reference brain coordinates. Detected neurons (from ***B***, ***C***) are then transformed to the reference atlas coordinate system. ***E1***, ***E2***, Coronal sections showing the Allen CCF 3.0 and locations of S1 and motor and somatosensory thalamic nuclei. Rt, Thalamic reticular nucleus; PL, ventroposterolateral nucleus. The positions of retrogradely labeled presynaptic neurons are marked with a yellow dot (***E1***) in an example SOM-Cre mouse injected in M1. Presynaptic neurons within ±0.1 mm of the plane are shown. ***E2*** is labeled to indicate registered thalamic areas. ***F1–3***, Injection site with starter cells in a SOM-Cre mouse. Merged image of green (***F2***) and red (***F3***) channels, showing yellow starter cells (***F1–3***, white arrowheads) and singly labeled cells (***F1***, blue arrows; ***F3***, yellow arrows). Green, TVA+ neurons (putative starter cells, ***F2***); Red, tdTomato+ neurons (putative presynaptic neurons, ***F3***). Right, Laminar distribution of PV+ and SOM+ somata, quantified as fraction of the total by layer. ***G***, ***H***, Example section (***G***, expanded in ***H***) showing retrograde label in S1 and thalamus from M1 starter cells in a PV-Cre mouse. Note S1 label and thalamic label. ***I***, ***J***, Example section showing retrograde label in S1 and thalamus from M1 starter cells in a SOM-Cre mouse. Note S1 label and thalamic label. ***K–N***, Cell detection examples in a SOM-Cre mouse. In cortex (***K***), detected cell somata are labeled with yellow circles (***L***). Example images for thalamus (***M–N***). ***O***, Quantification of presynaptic neuron location from brains aligned to the Allen CCF V3.0. Fraction of the total presynaptic neuron population (±SEM) plotted for all M1 injections in PV-Cre ($N = 5$, red) and SOM-Cre ($N = 4$, blue) mice. Dashed lines represent individual cases; solid line represents mean. Green dashed line, threshold for testing. *t test, $p < 0.05$ (gray asterisk, not significant when controlling for false discovery rate). ***P***, Quantification of thalamic inputs for all M1 injections in PV-Cre ($N = 5$, red) and SOM-Cre ($N = 4$, blue) mice. Data plotted as in ***O***, subdivided into distinct thalamic nuclei.

potassium gluconate-based internal solution containing the following (in mM): 128 potassium gluconate, 4 $MgCl_2$, 10 HEPES, 1 EGTA, 4 Na_2ATP, 0.4 Na_2GTP, 10 sodium phosphocreatine, and 3 sodium L-ascorbate, pH 7.27, 287 mOsm). These recordings targeted neurons in whisker M1 for whiskers (vM1, coordinates in Table 1). In some experiments, biocytin was added to the intracellular solution (3 mg/ml biocytin or neurobiotin). For subcellular ChR2-Assisted Circuit Mapping (sCRACM) experiments (Petreanu et al., 2009), TTX (1 μM, Tocris Bioscience), 4-AP (0.1–0.3 mM, Sigma-Aldrich), and 3-(2-carboxypiperazin-4-yl)propyl-1-phosphonic acid (CPP; 5 μM, Tocris

Table 1. Injection coordinates

Target	AP	ML	DV
Primary whisker motor cortex (vM1)	+1.1	0.9	0.5/0.8
Posterior thalamus (PO)	−1.2	1.3	2.75
Primary whisker somatosensory cortex (vS1)	−0.6	3.0	0.5/0.8
For rabies tracing			
Secondary motor cortex (M2)	+2.6	1.0	0.5/0.8
Forelimb motor cortex (fM1)	+0.6	1.5	0.5/0.8
Primary whisker somatosensory cortex (vS1)	−0.6	3.0	0.5/0.8

AP, Anterior/posterior axis reported relative to bregma (positive values anterior to bregma); ML, medial/lateral axis reported relative to the midline; DV, dorsal/ventral axis, depth from pia. Injections were made at both depths in cortex. Distances in mm.

Table 2. Mouse lines

Mouse lines	Line no.	Reference
PV-Cre	JAX 008069	Hippenmeyer et al. (2005)
SOM-Cre	JAX 013044	Taniguchi et al. (2011)
Ai14	JAX 007914	Madisen et al. (2010)
NK1R-CreER	JAX 035046	Huang et al. (2016)

Table 3. Viral reagents

Virus	Serotype	Addgene no.
CAG-ChR2-mVenus	AAV1, AAV9, and AAV10	20071
hSyn-Chronos-GFP	AAV1, AAV5, and AAV9	59170
CaMKIIa-hChR2(H134R)-EYFP	AAV9	26969
DIO-TVA-EGFP-B19G	AAV1	52473
N2c-ΔG-EnvA-tdTomato	CVS-N2c rabies	n/a

Bioscience) were added to the bath. Dose response of 4-AP concentration was confirmed in a subset of experiments comparing EPSC amplitude while 4-AP was added. Under these conditions, laser pulses (1 ms) depolarized ChR2-expressing axons in the vicinity of the laser beam and triggered the local release of glutamate. Measurements of postsynaptic currents then revealed the presence of functional synapses between ChR2-expressing axons and the recorded neuron near the photostimulus. Blocking action potentials prevented polysynaptic contributions.

Data were acquired at 10 kHz using an Axopatch 700B (Molecular Devices) and Ephus software (Suter et al., 2010) on a custom-built laser scanning photostimulation microscope (Shepherd et al., 2003). During sCRACM mapping, neurons were held at −70 mV. A blue laser (473 nm, CrystaLaser) was controlled via scan mirrors (Cambridge Technology). Light pulses were controlled with a shutter (4 ms open time) in series with an acousto-optic modulator (1 ms pulse, QuantaTech) to deliver ~0.5–2 mW at the specimen plane through a low-power objective (UPlanApo 4×, 0.16 NA, Olympus). Laser power was constant during a given day. Sweep consisted of 100 ms baseline and 300 ms following onset of the stimulus. The map grid (12 × 26 sites at 50 µm spacing) was centered horizontally over the soma of the recorded neuron, aligned at its upper edge to the pia, and covered the entire interneuron dendritic arbor. Maps were repeated 2–4 times and averaged across trials. Stimuli for short-term plasticity were delivered using 1 ms flashes of a 470 nm LED (Cairn). Sweeps were interleaved and repeated 4–6 times per stimulus frequency.

Data analysis. Electrophysiology data were low-pass filtered (1 kHz). EPSCs were detected with a threshold of >6× SD from baseline. Mean EPSC amplitude for input maps was averaged over a 75 ms poststimulus window (reported in pA). For comparison between cells in the same slice, total input was computed by summing supratheshold pixels. Paired comparisons across cells use the nonparametric Wilcoxon signed-rank test. Mean ratio of excitation were calculated as geometric means, with the strongest input layer shown as 1.0. In these comparisons, the bar graph was overlaid with a line showing the bootstrap mean and SD (10,000 replicates) resampling the paired data. To compare the axonal profile of S1 and PO axons (Fig. 1), we quantified the fluorescence as before (Hooks et al., 2013) by determining the mean fluorescence of pixels at a given laminar depth (binned in 50 bins across cortex from pia to white matter). Number of mice used for circuit mapping are the following: $N = 15$ (S1 to M1 PV+), $N = 12$ (PO to M1 PV+), $N = 10$ (S1 to M1 SOM+), $N = 10$ (PO to M1 SOM+), $N = 4$ (S1 to M1 Tacr1+), and $N = 4$ (PO to M1 Tacr1+). For short-term plasticity, we used the related-samples Wilcoxon signed-rank test for comparisons across pulses and across frequencies within the same connections. For comparisons across input type (S1/PO) and postsynaptic cell type (PV/SOM), we used the independent-samples Mann–Whitney U test in IBM SPSS Statistics software (version 28.0.1.1). Numbers are reported in figures for number of cells.

Data Availability

Data analysis was performed with custom routines written in MATLAB. Data acquisition and analysis software (M files in MATLAB format) is available on request.

Results

Anatomical tracing of long-range inputs to PV+ and SOM+ neurons

Incoming cortical and thalamic excitation to M1 directly excites pyramidal neurons and interneurons, evoking disynaptic feedforward inhibition. The interneurons carrying this feedforward inhibition likely include PV+ basket cells as well as SOM+ neurons. Conventional retrograde tracers can identify presynaptic cortical (Reep et al., 1990; Rouiller et al., 1993; Dum and Strick, 2002; Hoffer et al., 2003) and thalamic inputs (Deschênes et al., 1998; Kuramoto et al., 2009; Ohno et al., 2012; Kuramoto et al., 2015) to M1 (Hooks et al., 2013; Oh et al., 2014; Zingg et al., 2014), but do not differentiate between cell types in M1 receiving the input. To quantify how specific populations of interneurons are targeted by incoming cortical and thalamic afferents, we used genetically identified interneurons as starter cells for monosynaptic retrograde tracing with rabies virus (Wickersham et al., 2007b; Callaway and Luo, 2015). This enabled us to quantitatively compare presynaptic labeling across starter neuron types (PV+ and SOM+ neurons) as well as across cortical areas.

Using PV-Cre or SOM-Cre mice, we infected Cre+ interneurons with AAV-DIO-TVA-EGFP-B19G to label potential starter neurons and make them express both TVA receptor (to enable infection with EnvA pseudotyped rabies virus) as well as the rabies coat protein B19G (Fig. 1*F2*). PV+ and SOM+ starter cells in these injections were not restricted to a single cortical layer but spanned cortical laminae (L2–L6). After 2 weeks to express the receptor, EnvA-pseudotyped CVS-N2c G-deleted rabies expressing tdTomato (Reardon et al., 2016) was injected in forelimb motor cortex (fM1, $N = 5$ for PV+, $N = 4$ for SOM+ mice; Table 1). Fixed brains were sectioned, immunoamplified, and imaged. The whole-brain image stacks were reconstructed (Fig. 1*A*). Cell detection was then performed for tdTomato+ neurons in NeuroInfo (MBF Bioscience) in each plane using an artificial neural network (Fig. 1*B–C*). The image stack was aligned to the Allen CCF V3.0 (Oh et al., 2014; Kuan et al., 2015) using the structural label Neurotrace (Fig. 1*D–E*, blue), enabling the assignment of voxels containing structures and cells to defined cortical and thalamic regions (Fig. 1*G–N*). In selecting a motor area for whole-brain tracing, fM1 was used because we thought the data would be useful to studies of motor plasticity and learning in this area as well as to align the data with the results of the large-scale cell type census from the Brain Initiative Cell Census Network using gene expression, anatomic

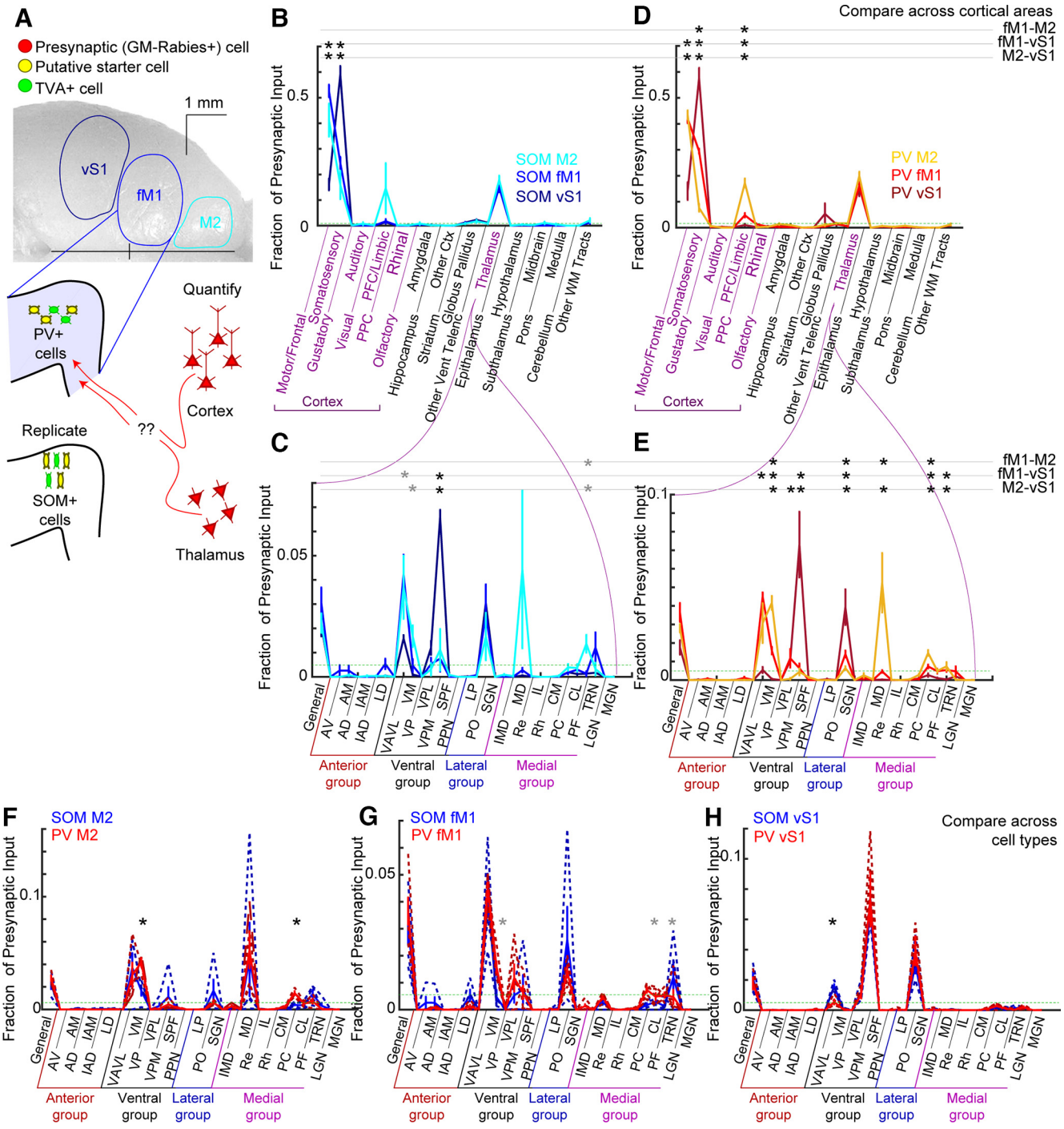

Figure 2. Monosynaptic retrograde tracing of inputs to PV+ and SOM+ neurons across cortical areas. ***A***, Schematic showing three dorsal cortical areas used for retrograde tracing from PV+ and SOM+ interneurons. In PV-Cre or SOM-Cre mice, injection of AAV expressing DIO-TVA-EGFP-B19G labels potential starter cells green in a Cre-dependent manner. This vector also expressed the TVA receptor to permit rabies uptake. Left, Subsequent injection of EnvA-pseudotyped CVS-N2c-tdTomato rabies labels starter cells yellow (red plus green); right, labels potential presynaptic partners red (in many cortical and thalamic areas). ***B–C***, Quantification of presynaptic neuron location for injections in SOM-Cre ($N = 4$, M2; $N = 4$, fM1; $N = 4$, vS1; cool colors) mice. Whole-brain image stacks were aligned to the Allen CCF V3.0. Presynaptic neuronal somata were detected and coordinates in CCF assigned to brain regions. Mean fraction of the total presynaptic neuron population (±SEM) plotted as in Figure 1. Quantification of inputs to all brain regions (***B***) and to thalamic nuclei (***C***). ***D–E***, Data from injections in PV-Cre ($N = 4$, M2; $N = 5$, fM1; $N = 5$, vS1; hot colors) plotted as in ***B***, ***C***. ***F–H***, Data of ***B–E*** replotted to compare input to SOM+ (blue) and PV+ (red) neurons in the same cortical locations, M2 (***F***), fM1 (***G***), and vS1 (***H***). Dotted lines represent individual cases; solid lines represent mean. Green dashed horizontal lines in ***B–H*** represent threshold for statistical comparison. Black asterisks represent significant differences (p value as indicated) after correcting for FDR. Gray asterisks represent comparisons not significant after correction for FDR.

projections, and physiology to define cell types in rodents and primates (Muñoz-Castañeda et al., 2021).

The distribution of presynaptic neurons was quantified by normalizing the number of cells detected in each brain region as a fraction of the total number of cells detected (Fig. 1*O*,*P*). The distributions were repeatable across different cases in the same brain region (Fig. 1*O*,*P*), which indicated that the NeuroInfo alignment was effective across individual brains and that the retrograde tracing method was reliable. To minimize excessive comparisons, we limited comparisons to brain regions where at

least one area exceeded a detection threshold (Fig. 1*O*,*P*, dotted line). Overall, the pattern was quite similar for inputs to PV+ and SOM+ neurons in M1. Most presynaptic inputs were found in cortex (Fig. 1*O*), in particular frontal and motor areas on the dorsal surface of cortex, as well as somatosensory cortex, which is strongly reciprocally connected to mouse M1 (Rocco-Donovan et al., 2011). About 20% of inputs for both interneuron classes were localized to thalamus, consistent with similar corticocortical and thalamocortical input to these cell types. We further examined the thalamocortical data by subdividing labeled neurons by thalamic nuclei (Fig. 1*P*). Thalamic nuclei associated with M1 based on prior anatomic studies were robustly represented, including ventroanterior/ventrolateral (VAVL), ventromedial (VM), and PO (Deschênes et al., 1998; Kuramoto et al., 2009; Ohno et al., 2012; Kuramoto et al., 2015). Note, although the Allen CCF V3.0 does not subdivide motor thalamus, the VAVL nucleus is heterogeneous and includes an anterior component that receives GABAergic input from basal ganglia (including substantia nigra) and a posterior component that receives excitatory input from the deep cerebellar nuclei (Kuramoto et al., 2009). Importantly, we did not detect significant differences between the number of neurons projecting to PV+ or SOM+ neurons after correction for false detection rate (Benjamini et al., 2009). Statistical power to detect such differences was limited by our number of observations, and subtle differences might emerge with more replicates.

We extended the retrograde viral tracing study to two other cortical areas strongly reciprocally connected with motor areas, primary somatosensory cortex, and M2. Experimental procedures were identical, except for the targeting of viral injections to different cortical areas in PV-Cre and SOM-Cre mouse lines. This enabled a comparison of M1 to areas with different cytoarchitecture and potentially different connectivity rules, that is, a primary sensory area (with a typical neocortical granular layer 4) and a frontal area (agranular and higher-order cortical area). We first made comparisons across cortical areas of starter cell within a given interneuron line (Fig. 2*B*–*D*). For SOM+ neurons, the major areas labeled were motor cortex and frontal cortex (greater in fM1 and M2 starter cases than in vS1 starter cases) and somatosensory cortex (greater in vS1 starter cases), with a relatively uniform fraction of thalamic input (~20%) across neocortical areas). PV+ input was similar, with the additional note of significantly greater input from limbic areas (mostly orbital cortex) to M2 than to other areas. Comparison of input from specific thalamic nuclei was considerably different across injection sites. In general, the pattern of thalamic label could be used to infer the cortical target, with a reasonably large number of nuclei providing a specific pattern of cortical input. For example, in cases using PV+ starter neurons, vS1 injections could be identified by more robust ventroposteromedial (VPM) and PO labeling. fM1 injections had strong input from VAVL and VM as well as PO and midline nuclei. M2 input was similar to that of fM1 in receiving strong VAVL and VM input but also received significant mediodorsal thalamic nucleus (MD) input (which vS1 and fM1 did not) as well as input from midline nuclei including PC and PF. This is consistent with substantial differences in thalamocortical targeting across cortical areas. However, in comparing input to different cell types within a given cortical area, few significant differences were detected. For M2, PV+ interneurons labeled more thalamic cells in VM and PC compared with SOM+ neurons in M2. In vS1, SOM+ interneurons labeled more VAVL neurons than PV+ neurons. For most nuclei, there were no detectable differences. In general, this was consistent with much larger differences in thalamic label for cortical areas than for specific cell types within a cortical area.

Synaptic mapping of long-range excitatory inputs from S1 and thalamus to M1

Because we had hypothesized that inputs to any cortical area would show specificity in layers and cell types targeted, we studied the layer-specific excitation from two major inputs to M1 from sensory cortex (S1) and thalamus (PO) using channelRhodopsin-based circuit mapping approaches. These studies focused on whisker M1 in lateral agranular areas for comparison to earlier studies using comparable methods to map input to pyramidal neurons. Prior work demonstrated that incoming cortical and thalamic excitation to M1 directly excites pyramidal neurons (Mao et al., 2011; Hooks et al., 2013). Our data showed that these inputs were capable of evoking disynaptic feedforward inhibition by recording from pyramidal neurons in M1 in brain slice while exciting ChR2+ axons from S1 at −70 mV and +0 mV and quantifying the EPSC and IPSC amplitudes, respectively (Fig. 3). The feedforward inhibition at +0 mV onset was ~2 ms slower than the excitation at −70 mV (Fig. 3*A*). Across M1 layers, excitation is matched to inhibition, with similar ratios across layers. The interneurons carrying this feedforward inhibition are unknown but are presumed to include PV+ basket cells. Further, it is likely that the GABAergic neurons carrying the disynaptic inhibition reside mainly in the same layer as the pyramidal neuron soma (Kätzel et al., 2011).

To identify the source of this disynaptic inhibition, we then quantified how specific populations of interneurons are targeted by incoming cortical and thalamic afferents. This experiment will also permit a direct comparison of functional synaptic connectivity by synaptic circuit mapping and anatomic tracing by retrograde viruses. We labeled axons from S1 or PO with ChR2-mVenus. Because thalamic injections label neurons in a sphere of ~0.5 mm, PO injections also include the posterior components of VL (cerebellar recipient motor thalamus), whose axonal projections to cortex were identical to PO in our prior study (Hooks et al., 2013). These axons arborized in distinct layers of cortex (Fig. 3*C*,*D*). We selected two populations of Cre-driver mice (PV-Cre and SOM-Cre) crossed to a tdTomato reporter (Ai14; Madisen et al., 2010) to label genetically defined interneurons across the thickness of M1.

We then targeted whole-cell recordings to tdTomato+ interneurons in M1 brain slices in the field of mVenus+ axon terminals. We used a 473 nm laser to excite ChR2+ axon terminals while recording in TTX, CPP, and 4-AP (sCRACM; Petreanu et al., 2007, 2009). TTX prohibited action potentials, ensuring inputs measured were monosynaptic. 4-AP slowed axon repolarization, allowing the ChR2-evoked EPSC to occur (Fig. 3*G*,*H*). CPP is a potent NMDAR antagonist used to block slow NMDAR currents and focus circuit mapping on kinetically rapid AMPAR glutamate receptors. Because we were concerned that axons targeting different cell types might vary in their responsiveness to 4-AP, we confirmed that addition of 4-AP in the presence of TTX restored synaptic release with similar effectiveness. These conditions do not mimic *in vivo* synaptic transmission and prevent normal kinetics in presynaptic axons. Instead, they are used to quantify synaptic connection strength in conditions that prevent *in vitro* plasticity and ensure only monosynaptic transmission is measured. In mapping experiments, a single interneuron was recorded while stimulating the brain slice with a 473 nm laser. A

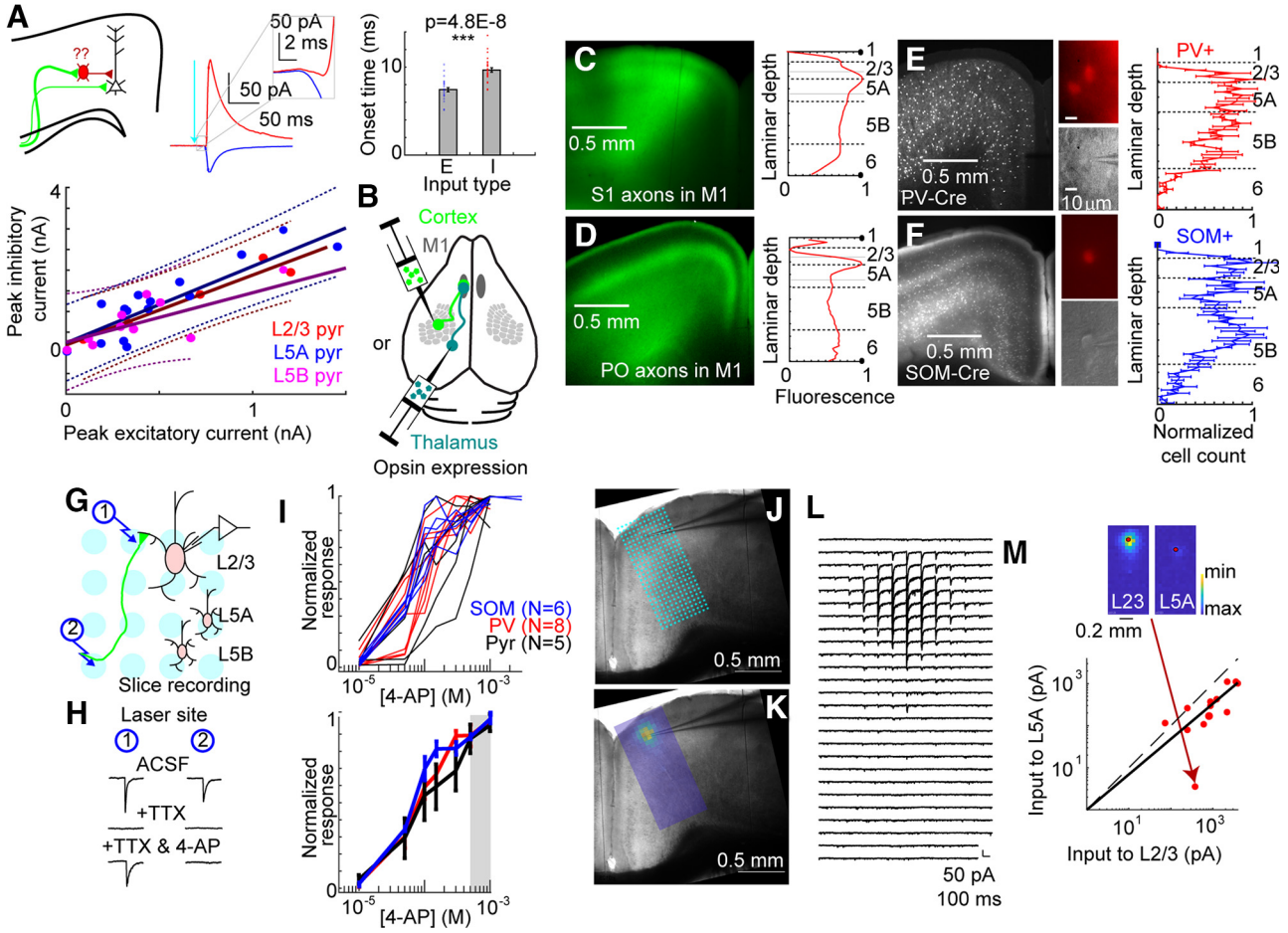

Figure 3. Mapping long-range excitatory inputs to mouse motor cortex interneurons. ***A***, Interneurons carry feedforward inhibition in M1. Whole-cell recordings at −70 mV (blue) and 0 mV (red) show optically induced feedforward inhibition from S1 inputs to M1 (bottom left) with a short latency difference (inset). Difference in latency between EPSC (blue) and IPSC (red) is plotted to compare onset (mean and SE; $N = 29$). EPSC and IPSC amplitudes are roughly proportional (right) across all cortical layers (bottom right). Linear fit and 95% confidence interval (dashed lines) plotted. ***B***, AAV vectors expressing optogenetic activators (ChR2 or Chronos) were stereotaxically injected into cortex (S1, light green) or thalamus (PO, dark green). ***C***, Left, mVenus+ axons from S1 arborize across layers of M1 in a columnar projection (4× image). Right, Fluorescence is highest in L5A (brightness quantified across cortical layers). ***D***, Left, mVenus+ axons from PO arborize across layers of M1 in two main layers. Right, Fluorescence is highest in L1 and the border of L/23 and L5A. ***E***, PV-Cre mice were crossed to a tdTomato reporter (Ai14), labeling interneurons across M1 in L2–L6. Postsynaptic interneurons were recorded across all layers for comparison. Inset, Fluorescence image 60× (top) and corresponding brightfield image (bottom) shows patch pipette on tdTomato+ neuron in PV-Cre x Ai14 mouse. Normalized laminar distribution of PV+ somata ($N = 5$ slices) measured at right. ***F***, SOM-Cre mice were crossed to a tdTomato reporter (Ai14), labeling interneurons across M1 in L2–L6. L1 signal represents tdTomato+ axons from SOM+ neurons. Postsynaptic interneurons were recorded across all layers for comparison. Right, Normalized laminar distribution of SOM+ somata ($N = 5$ slices) measured. ***G***, Targeted whole-cell recordings in brain slice were made from interneurons while stimulating with a 473 nm laser at different points, shown in light blue. Full grid illustrated as in ***J***. ***H***, Stimulation of 473 nm excites axons at example points 1 and 2, but TTX addition extinguishes responses. Addition of 4-AP permits local release at points where opsin+ axons contact interneuron dendrites (point 1) but not distant points along the axon (point 2). ***I***, Similar concentrations of 4-AP are required to restore synaptic responses regardless of postsynaptic neuron type. Pyr, Pyramidal neuron. Top, Individual cells are plotted; bottom, average and SE are plotted. Gray box represents [4-AP] used for mapping. ***J***, Typical input mapping experiments sampled a 12 × 26 point grid with points spaced at 50 mm and aligned to the pia. Brightfield image (4×) shows recording pipette in M1. ***K***, Heat map shows stronger responses (red) near the soma of the recorded neuron. ***L***, Example traces for a L2/3 PV+ neuron show location of input. ***M***, Inset, Two maps are shown to compare input between L2/3 and L5A PV+ interneurons. The summed synaptic input across the map is compared for each cell pair recorded in the same slice. Arrow indicates a point from one L2/3–L5A pair. Dashed line represents $y = x$ (similar input to both layers); solid line represents the geometric mean of the L2/3 and L5A input strength, presented as a line of equivalent slope.

12 × 26 grid (Fig. 3*J*) was used for stimulation, resulting in evoked EPSCs (Fig. 3*L*) that differed in amplitude depending on the location of the laser stimulus. This method activates synapses within ~0–75 μm of the flash (Supplementary Petreanu et al., 2009, their supplementary Fig. 3). A heat map showing the size of the response was then plotted on top of the cell location in the slice (Fig. 3*K*). We compared each pair of interneurons in different layers recorded in the same slice, summing the EPSC amplitude across the map. This measure of input strength was used to compare EPSC amplitude across layers (Fig. 3*M*). Thus, our comparisons of input strength (Figs. 4-7) required pairwise comparison of neurons recorded in the same slice to normalize for ChR2 expression between animals, and nonparametric statistics were used to avoid assumptions about the distribution of connection strength.

S1 targeting of PV+ and SOM+ interneurons in M1

First, we recorded from tdTomato+ PV+ interneurons in the whisker region of M1 in PV-Cre x Ai14 mice. S1 inputs to M1 mainly targeted PV+ interneurons in L2/3. L2/3 PV+ neurons received more than twice as much input than any other layer. All PV+ neurons ($N = 58$) in all layers were plotted for comparison (Fig. 4*B*), with each map reduced to a column vector by summing the input map across rows. Most responsive cells and the strongest responding cells were found in L2/3. A pairwise comparison of L2/3 with other PV+ neurons recorded in the same

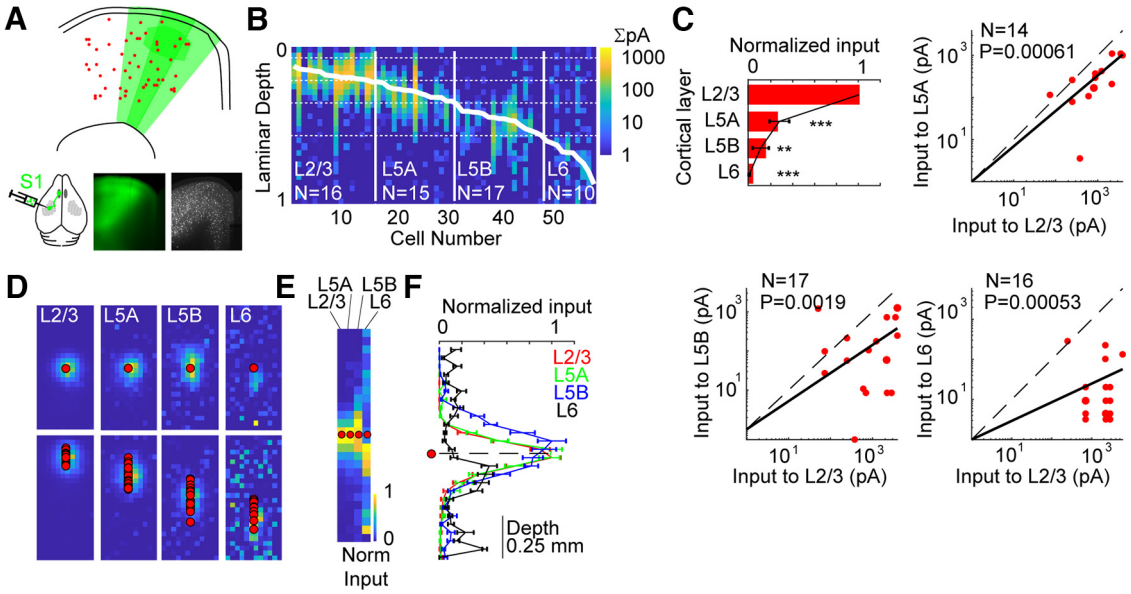

Figure 4. S1 input to M1 targets upper layer PV+ neurons. ***A***, Diagram showing PV+ neurons (red) in GFP+ axons from S1. ***B***, S1 input to M1 PV+ neurons across layers ($N = 58$ total). Each cell is represented as a single column (vector), with the rows of the input mapped summed and aligned to the pia. Diagonal white line represents the soma location for that cell. Vertical white lines represent layer divisions. Horizontal dotted lines represent approximate laminar borders. Synaptic strength (summed, in nA) for each location in depth are represented by the heat map (scale at right). Laminar depth is normalized to 0 = pia, 1 = white matter. ***C***, Strength of synaptic input. The bar represents the geometric means of the amplitude ratio, normalized to the layer receiving the strongest input (L23). The overlaid graph shows the mean ratio and SD (based on 10,000 replicate bootstrap). Adjacent to the summary, three graphs for comparison of input strength across neurons in different cortical layers. Each point represents input to a pair of neurons in the same slice (circle for each neuron). Dashed line represents unity. N, Number of pairs; *p* value, Wilcoxon signed-rank test. ***D***, Maps of synaptic input location in the dendritic arbor for PV+ neurons in each layer. Top row, Normalized soma-centered map (maps registered to soma center across cells). Bottom row, Normalized pia-aligned maps. Normalized maps are noisy when input is weak. ***E***, ***F***, Input location summarized for all four layers. Normalized mean input maps were averaged into a vector (***E***) and aligned to the soma (red circle). These were graphed with mean and SD (***F***), showing input relative to the soma in 50 mm bins. Dashed line indicates soma depth. $*p < 0.05$, $**p < 0.01$, and $***p < 0.001$.

slice showed that L5A neurons received only ~30% the input of L2/3 PV+ neurons ($p < 0.001$). Similarly, input to L5B and L6 was even weaker (Fig. 4*C*). This input was mostly centered around the interneuron soma, as shown in maps where the grid is aligned to the soma (Fig. 4*D*,*E*). For layers with weaker input, noise is increased in normalized input maps (Fig. 4*D*, L6).

We repeated this experiment for S1 inputs to SOM+ interneurons, using SOM-Cre x Ai14 mice (Fig. 5). As in PV-Cre mice, SOM-Cre labeled interneurons across the cortical thickness, allowing a fair comparison of input strength across layers. Here, S1 inputs most strongly targeted L5A interneurons. L2/3 SOM+ neurons only received ~30% the input of L5A SOM+ cells (Fig. 5*C*, $p < 0.05$). Some neurons in upper L5B received stronger input, whereas deeper neurons received less (Fig. 5*B*); overall, this was not significantly different from L5A ($p = 0.067$). L6 SOM+ neurons received the least input ($p < 0.01$). As with PV+ neurons, S1 input was generally perisomatic, especially for L2/3 SOM+ cells. However, the center of mass of the input was shifted below the soma toward white matter for SOM+ cells in L5A, 5B, and L6 (Fig. 5*D–F*), suggesting that S1 axons were capable of targeting different subcellular domains in different interneuron types.

PO targeting of PV+ and SOM+ interneurons in M1

Next, we repeated these experiments while labeling thalamic inputs from PO nucleus of thalamus, a higher-order somatosensory nucleus whose input to M1 pyramidal neurons had been characterized (Hooks et al., 2013, 2015). Thalamic injections were determined in individual animals to be in PO and the adjacent portions of posterior motor thalamus by the presence of axonal fluorescence in L1 and at the border of L2/3 and L5A. The absence of L5B fluorescence in these animals confirmed that our injections did not target the anterior components of the VAVL complex, which had previously been shown to arborize in three distinct bands, adding L5B to the pattern described above (Hooks et al., 2013). Targeting recordings to tdTomato+ PV+ interneurons within the arborization of PO axons, we found that in contrast to S1 inputs, neurons in L5A received the strongest synaptic input (Fig. 6*C*). However, input to PV+ cells in the top three layers of motor cortex (L2/3, L5A, and L5B) was generally strong, without significant differences. Only synaptic input to L6 was weaker ($p < 0.05$). This input was not centered on the soma in the dendritic arbor but instead was generally targeted to the deep (white matter) side of proximal dendrites (Fig. 6*D–F*). This was the case for all four layers measured (L2/3, L5A, L5B, and L6).

Variability in synaptic input from PO inputs to SOM+ interneurons made estimating a mean response difficult. We used the same approach (Fig. 7) to quantify synaptic input. However, the pattern of input to SOM+ was noisy and did not match any previous pattern observed for the other GABAergic cells (Figs. 4-6) nor pyramidal neurons previously recorded (Mao et al., 2011; Hooks et al., 2013). Instead, we found that L5B was the most strongly excited layer (Fig. 7*C*), with significantly reduced input in L5A ($p < 0.001$). Comparisons to L2/3 and L6 were not significant and showed quite different patterns across different cells, with some pairs favoring L2/3 or L6 and others favoring L5B. The subcellular localization of input was also heterogeneous, with some SOM+ neurons in L5B and L6 receiving input in basal dendrites shifted toward white matter from the soma (Fig. 7*D–F*).

Using this circuit mapping approach gives a direct means to compare subcellular localization of synaptic input in the

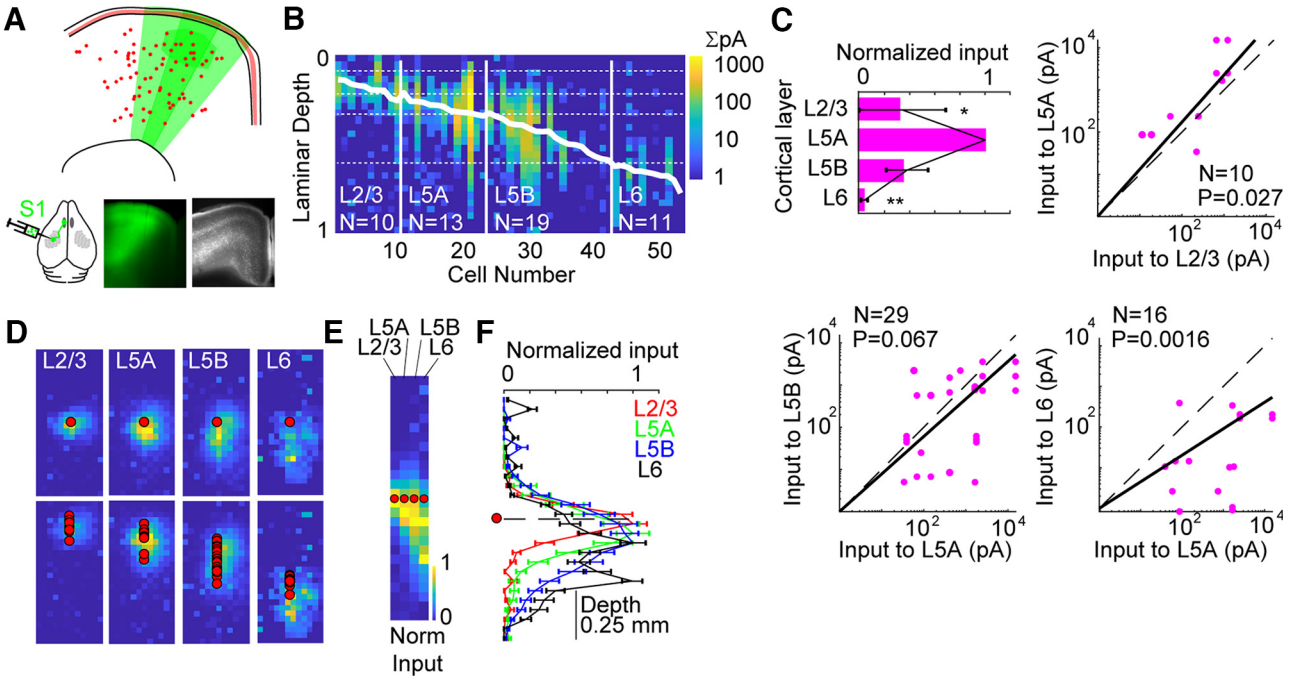

Figure 5. S1 input to M1 targets middle layer SOM+ neurons. ***A***, Diagram showing SOM+ neurons (red) in GFP+ axons from S1. ***B***, S1 input to SOM+ neurons across layers ($N = 53$ total). Each cell is represented as a single column (vector), with the rows of the input mapped, summed, and aligned to the pia. Diagonal white line represents the soma location for that cell. Vertical white lines represent layer divisions. Horizontal dotted lines represent approximate laminar borders. Synaptic strength (summed, in nA) for each location in depth are represented by the heat map (scale at right). Laminar depth is normalized to 0 = pia, 1 = white matter. ***C***, Strength of synaptic input. The bar represents the geometric means of the amplitude ratio, normalized to the layer receiving the strongest input (L5A). The overlaid graph shows the mean ratio and SD (based on 10,000 replicate bootstrap). Adjacent to the summary, three graphs for comparison of input strength across neurons in different cortical layers. Each point represents input to a pair of neurons in the same slice (circle for each neuron). Dashed line represents unity. N, Number of pairs; *p* value, Wilcoxon signed-rank test. ***D***, Maps of synaptic input location in the dendritic arbor for SOM+ neurons in each layer. Top row, normalized soma-centered map (maps registered to soma center across cells). Bottom row, normalized pia-aligned maps. Normalized maps are noisy when input is weak. ***E***, ***F***, Input location summarized for all four layers. Normalized mean input maps were averaged into a vector (***E***) and aligned to the soma (red circle). These were graphed with mean and SD (***F***), showing input relative to the soma in 50 mm bins. Dashed line indicates soma depth.

dendritic arbor of postsynaptic neurons. This insight is constrained by methodological limitations of patch clamp, which limit our ability to study distal dendrites. Reducing connectivity to a single number for strength is imperfect because inputs vary in receptor kinetics and local conductances. Interneurons, however, are generally more electronically compact than pyramidal neurons, with higher input resistance (Scala et al., 2021). Further, the subcellular targeting data (Figs. 4-7*D–F*) shows that there are not major shifts in the input location to PV+ and SOM+ interneurons, with these inputs being close to soma centered, although some mechanisms for afferent targeting exist and may differ between interneuron subtypes. S1 input to PV+ neurons is evenly distributed perisomatically, whereas these same afferents tend to target dendrites ~50–150 µm below the soma of SOM+ cells. Similarly, PO input to PV+ cells is also shifted deep to the soma center by ~50–150 µm. This offset is in contrast to thalamic inputs to pyramidal neurons (Petreanu et al., 2009), where PO input targets the apical dendrites, and especially the L1 arbors of L3 pyramidal neurons but is soma centered (and quite strong) for L5A pyramidal neurons. Thus, different cell types may direct input from a defined presynaptic pathway to a small extent within their arbors.

Complementary patterns of input to specific interneuron types

By comparing synaptic strength across layers and normalizing excitability to the strongest input layer for multiple cell types, we were able to compare the pattern of input for the same pathway to multiple cell types. We plotted the normalized input strength graph on the same axes for S1 inputs or PO inputs to PV+ and SOM+ cells, as well as the same data grouped by input to PV+ or SOM+ cells (Fig. 8*A–D*). This enabled a direct comparison of S1 and PO input to PV+ and SOM+ neurons. Here, the same presynaptic afferents preferred interneurons of different types in different layers. Considering the data organized by postsynaptic target, cortical inputs from S1 to PV+ cells strongly preferred the uppermost (L2/3) PV+ cells, whereas the functional targeting of PO inputs was biased toward deeper layers (L5A and L5B; Fig. 8*C*). Input to SOM+ neurons showed a similarly complementary pattern, with input from S1 axons most strongly exciting L5A, which is the layer least strongly excited by PO (Fig. 8*D*). Thus, the same type of interneuron is targeted in a different manner by the cortical and thalamic inputs. For comparison, we plotted the input strength to excitatory neurons (Hooks, 2017). The published data show that S1 and PO most strongly target pyramidal neurons in layers L2/3 and L5A (Porter et al., 1990), with a roughly similar pattern (Fig. 8*E*). We summarize all the synaptic strength experiments schematically in Figure 8*F*, where arrow thicknesses to specific cell types indicate cell-type specific connectivity.

Because SOM+ neurons comprise a diverse range of neurons, including Martinotti and non-Martinotti subsets (Tremblay et al., 2016), we were curious whether the input pattern to the SOM+ neurons labeled in our SOM-Cre x Ai14 strategy would be able to be replicated in a more targeted subset of cells (Huang et al., 2016; Tasic et al., 2018). SOM neurons had shown variability, especially for thalamic inputs. SOM+ neurons include at least two (and likely more) molecular subtypes (Ma et al., 2006;

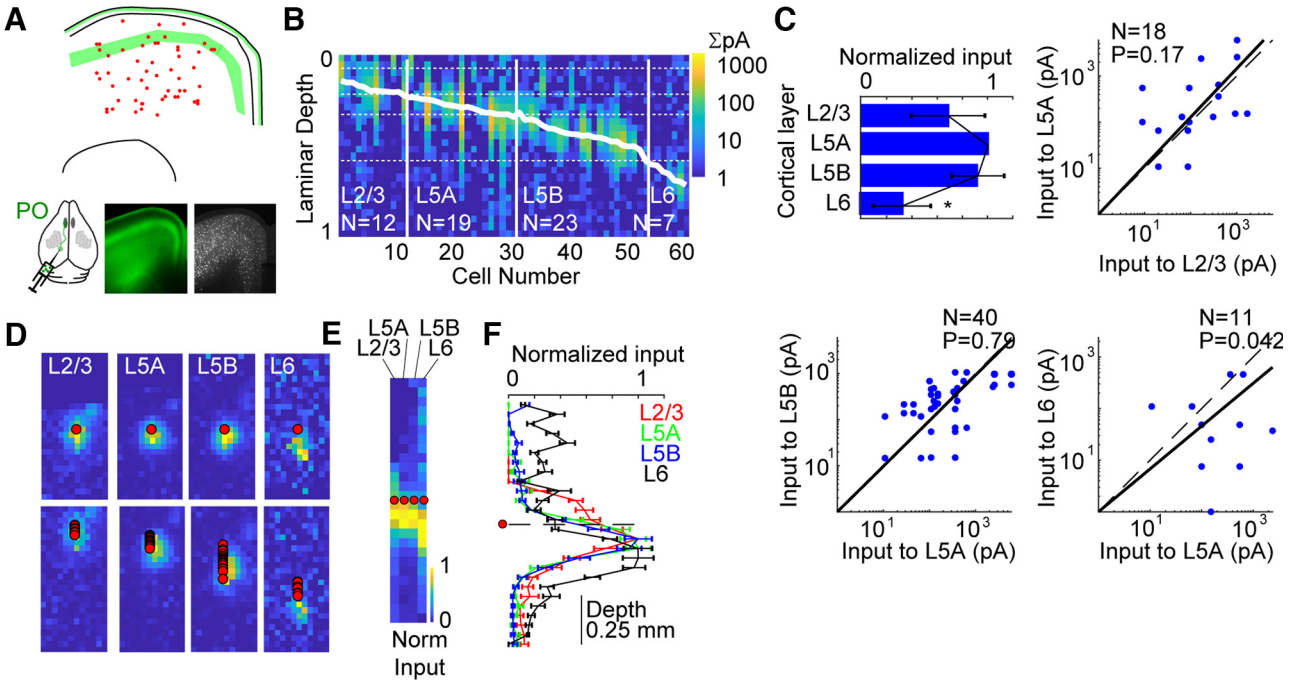

Figure 6. PO input to M1 PV+ neurons targets upper and middle layers. ***A***, Diagram showing PV+ neurons (red) in GFP+ axons from PO. ***B***, PO input to PV+ neurons across layers (N = 61 total). Each cell is represented as a single column (vector), with the rows of the input mapped, summed, and aligned to the pia. Diagonal white line represents the soma location for that cell. Vertical white lines represent layer divisions. Horizontal dotted lines represent approximate laminar borders. Synaptic strength (summed, in nA) for each location in depth are represented by the heat map (scale at right). Laminar depth is normalized to 0 = pia, 1 = white matter. ***C***, Strength of synaptic input. The bar represents the geometric means of the amplitude ratio, normalized to the layer receiving the strongest input (L5A). The overlaid graph shows the mean ratio and SD (based on 10,000 replicate bootstrap). Adjacent to the summary, three graphs for comparison of input strength across neurons in different cortical layers. Each point represents input to a pair of neurons in the same slice (circle for each neuron). Dashed line represents unity. N, Number of pairs; p value, Wilcoxon signed-rank test. ***D***, Maps of synaptic input location in the dendritic arbor for PV+ neurons in each layer. Top row, normalized soma-centered map (maps registered to soma center across cells). Bottom row, normalized pia-aligned maps. Normalized maps are noisy when input is weak. ***E***, ***F***, Input location summarized for all four layers. Normalized mean input maps were averaged into a vector (***E***) and aligned to the soma (red circle). These were graphed with mean and SD (***F***), showing input relative to the soma in 50 mm bins. Dashed line indicates soma depth.

Zeisel et al., 2015; Tasic et al., 2018; Naka et al., 2019), which might account for the variability in the data. One subset of SOM+ interneurons expresses Tacr1, as well as NPY and nNOS (Kubota et al., 2011), although these have differences in nNOS expression level (Dittrich et al., 2012).

Thus, we labeled the Tacr1+ subset of interneurons using a NK1R-CreER mouse crossed to a tdTomato reporter. Tacr1+ cells, like both PV+ and SOM+ neurons, are present across cortical layers 2–6. This made comparison of input strength possible. This was not the case for VIP+ neurons, which are much more numerous in only upper layers (~60% in L2/3; Prönneke et al., 2015), as well as other non-VIP expressing 5HT3aR+ interneurons that are similarly biased to L1 and L2/3 (Lee et al., 2010). We repeated our input mapping experiments in a limited number of NK1R-CreER mice, which label Tacr1+ cells, and presented the data in a similar format. Because of limited numbers of cells, these conclusions are not as strong as the PV+ and SOM+ mapping experiments. This presented a pattern of input strength quite in contrast to that of the SOM-Cre x Ai14 mice (Fig. 8*H*,*I*). In particular, S1 input had been distributed across L2/3, L5A, and L5B to SOM+ neurons, but most strongly to L5A. In contrast, this subset had a quite distinct pattern. Tacr1+ cells responded well to S1 inputs across multiple layers. Of note, the strongest responses were in in L2/3 and L6, with weaker input to L5 (Fig. 8*F*–*H*). The input from PO was noisy and also did not correspond to the SOM+ pattern, with strongly responding neurons in L5A and L5B. This emphasized the likelihood that each molecular subtype of interneuron has distinct mechanisms to govern synaptic strength. This variability could be quite significant, given that there are potentially as many as 50 distinct cortical interneuron populations (Muñoz-Castañeda et al., 2021). Because whole-cell methods for circuit mapping are necessarily limited to recording small numbers of cells per brain slice, studying connectivity and plasticity for smaller cortical neurons populations would benefit from higher throughput methods.

Because our inputs to PV+ and SOM+ neurons were quantified as normalized input strength, we wondered whether the absolute strength of input to PV+ and SOM+ differed across pathways. We compared input across pathways and cell types by plotting the absolute input strength for all cells on the same scale, as other investigators have done (Kinnischtzke et al., 2014). This was done by summing the EPSC amplitudes across the points of the input map, as in Figure 3*L*. Cell vector plots were presented as before (Fig. 8*G*) using the same logarithmic scale for all plots to improve presentation of more frequent recordings with weaker inputs. In general, excitatory input from S1 and PO to either interneuron type (PV+ or SOM+, top and middle row) was of similar magnitude. Averaging input by layer confirmed that monosynaptic input was of comparable strength (Fig. 8*I*). The overall pattern is similar to our normalized data. The distribution of S1 and PO input to PV+ is nearly overlapping, with the exception of input to L2/3 PV+ neurons. Input to SOM+ neurons is of similar strength from S1 and PO except for L5A, where the absence of thalamic input is pronounced. Corticocortical input is similar or stronger to SOM+ neurons than PV+ neurons at each laminar depth except L2/3. Thalamocortical

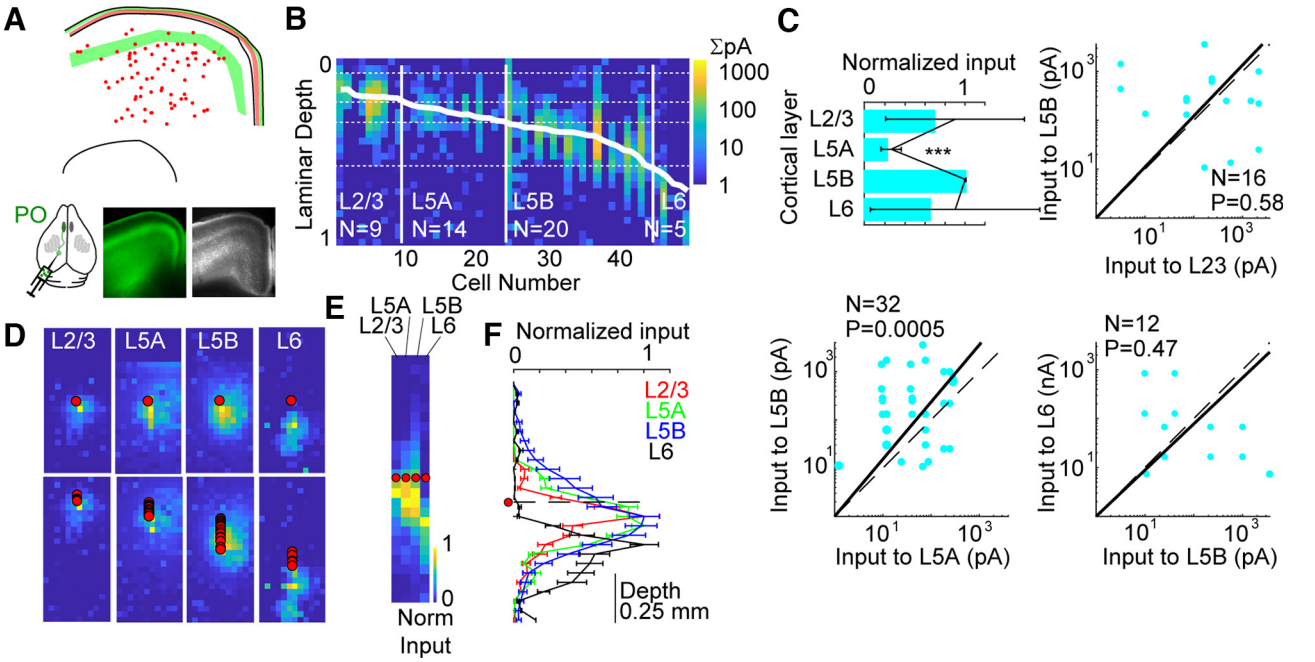

Figure 7. PO input to M1 SOM+ neurons is variable. ***A***, Diagram showing SOM+ neurons (red) in GFP+ axons from PO. ***B***, PO input to SOM+ neurons across layers ($N = 48$ total). Each cell is represented as a single column (vector), with the rows of the input mapped, summed, and aligned to the pia. Diagonal white line represents the soma location for that cell. Vertical white lines represent layer divisions. Horizontal dotted lines represent approximate laminar borders. Synaptic strength (summed, in nA) for each location in depth are represented by the heat map (scale at right). Laminar depth is normalized to 0 = pia, 1 = white matter. ***C***, Strength of synaptic input. The bar represents the geometric means of the amplitude ratio, normalized to the layer receiving the strongest input (L5B). The overlaid graph shows the mean ratio and SD (based on 10,000 replicate bootstrap). Adjacent to the summary, three graphs for comparison of input strength across neurons in different cortical layers. Each point represents input to a pair of neurons in the same slice (circle for each neuron). Dashed line represents unity. N, Number of pairs; *p* value, Wilcoxon signed-rank test. Plots show substantial heterogeneity. ***D***, Maps of synaptic input location in the dendritic arbor for SOM+ neurons in each layer. Top row, normalized soma-centered map (maps registered to soma center across cells). Bottom row, normalized pia-aligned maps. Normalized maps are noisy when input is weak. ***E***, ***F***, Input location summarized for all four layers. Normalized mean input maps were averaged into a vector (***E***) and aligned to the soma (red circle). These were graphed with mean and SD (***F***), showing input relative to the soma in 50 mm bins. Dashed line indicates soma depth.

input is stronger to L5A PV+ neurons than to SOM+ cells. Outside of this layer, however, input strength to SOM+ cells is equal to PV+ neurons.

Excitation and inhibition ratio for corticocortical and thalamocortical afferents

Circuit mapping studies thus permit the estimation of incoming excitation and inhibition from long-range inputs to M1. Monosynaptic excitation from S1 to pyramids across cortical layers is plotted as a ratio across layers (Fig. 9*A*), using published data (Mao et al., 2011). An estimate of recruited inhibition is made based on the monosynaptic excitation from S1 to either PV+ or SOM+ neurons in the same layers. Then the E/I ratios across layers are computed (Fig. 9*B*). Excitation and inhibition for PO (Fig. 9*C*,*D*) is estimated in a similar way using published data (Hooks et al., 2013). These datasets are selected because the methods are comparable.

These results suggest that there is not a lot of sensitivity to which method is used to quantify E/I ratio. Using PV or SOM is coarsely similar. The pattern depends on presynaptic input. S1 input generally shows E/I ratio greater than one, with a gradual increase with cortical depth. But PO input generally shows E/I ratio less than one, with a gradual decrease with cortical depth. S1 E/I ratio in L5B is at a local minimum, suggesting that L5B is the least likely to be excited by this input. This suggests that S1 input may inhibit most descending output or be selective about which output can pass. Similarly, the E/I ratio in both L5B and L6 is lowest for PO input. This similarly suggests that thalamic input is also likely to inhibit most descending output, perhaps more so than S1 because of the lower E/I ratio. Overall, the E/I ratio emphasizes the preference of S1 and PO input to excite certain layers, such as L2/3 and L5A, while maintaining inhibition relatively high in L5B. Notably, E/I ratio for L6 is relatively high for S1 input but quite low for PO input, but the significance of this disparity is unclear.

Direct comparison of synaptic and anatomic connectivity

We sought to make a quantitative comparison between input to PV+ and SOM+ neurons as measured by physiological and anatomic experiments. Differences in how the data are quantified presented challenges. Figure 10 describes the methodology by which this comparison was made. Because the presynaptic neurons labeled by monosynaptic tracing might connect to a starter cell in any cortical layer, we considered our anatomic tracing data to present an averaged view of connectivity to specific interneurons across all cortical layers. To make this data comparable to our physiological data where target PV+ and SOM+ neurons were more explicitly identified by laminar position, we sought to derive an average connection strength to PV+ or SOM+ neurons by converting the layer-by-layer strength of synaptic connectivity (Fig. 10*A*, left) into a weighted average strength (Fig. 10*A*, at bottom) using the fractional distribution of PV+ and SOM+ neurons (potential starter neurons) in each layer (Fig. 10*A*, middle) as weighting factors. This not only determined the weighted average, but also by resampling the individual neurons recorded in each category, a bootstrap mean could be determined to assess variability of this estimate of physiological connectivity. This is presented as mean ± SEM in the bottom for the graphs in Figure 10*A*; the scattered points in Figure 10*C* represent

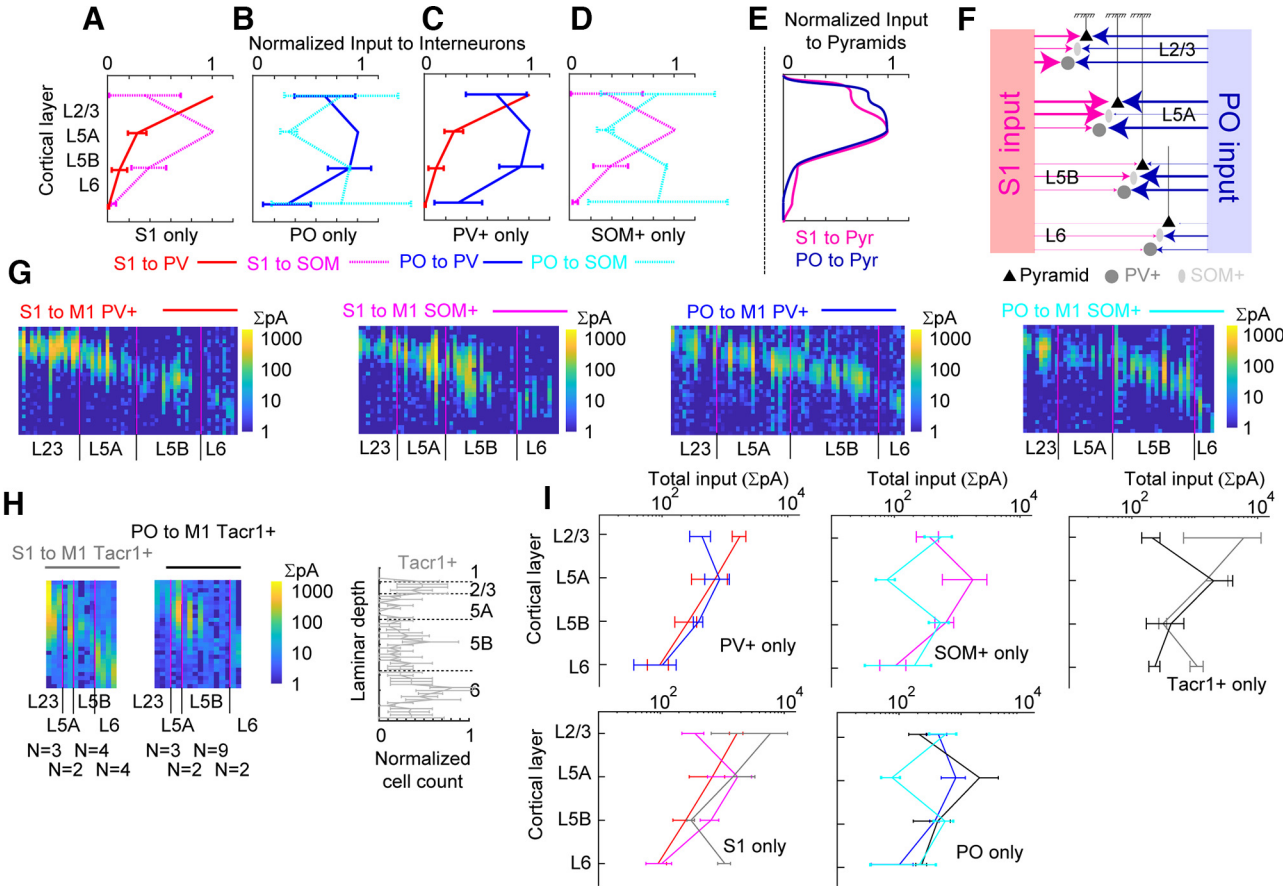

Figure 8. Complementary patterns of input to specific interneuron types. ***A–D***, Summary graphs comparing the distribution of excitatory input to PV+ and SOM+ neurons. These plots compare normalized input from (***A***) S1 only or (***B***) PO only to PV+ and SOM+ neurons. ***C***, ***D***, Compare input to PV+ only (***C***) or SOM+ only interneurons. ***E***, The pattern of normalized input strength to pyramidal neurons (Pyr) from S1 and PO, after Mao et al. (2011) and Hooks et al. (2013). ***F***, Diagram summarizing input maps. ***G***, Absolute input strength for S1 and PO inputs, plotted as input vectors on a log scale. From left to right, S1 input to PV+ and SOM+ neurons and PO input to PV+ and SOM+ neurons. ***H***, Tacr1+ neurons (a subset of SOM+ neurons) presented in a similar fashion. Left, input maps from S1 and PO. For Tacr1+ neurons, $N = 3/2/4/4$ for S1 input to L2/3, L5A, L5B, and L6; $N = 3/2/9/2$ for PO input. Normalized laminar distribution of Tacr1+ somata ($N = 4$ slices) measured at right. ***I***, Absolute input strength averaged by layer and plotted on a log scale for comparison between S1 and PO inputs (top row) to different interneuron types. Bottom row, Comparison of either S1 or PO input to different interneuron types presented on the same axes.

replicates. The weighted average quantified the relative input strength to PV/SOM from cortical (0.7842) and thalamic (1.3724) input. This suggested that monosynaptic thalamic input slightly favored PV+ neurons, whereas corticocortical input might favor SOM+ neurons, likely because the strongest recipient layers for SOM+ (L5A and L5B) contained larger numbers of cells that the strongest PV+ recipient layer (L2/3). A ratio of PV/SOM input based on anatomic tracing (Fig. 10*B*) could also be determined. We quantified the mean fraction of presynaptic input in somatosensory cortex or thalamus. Using this as an anatomic connection strength, we then made a ratio between PV and SOM as done for synaptic input. Anatomical input from both somatosensory cortex (PV/SOM, 1.2045) and thalamus (1.0853) slightly favored PV+ neurons in M1. To explore the degree to which these ratios varied, we compared $N = 1000$ bootstrap replicates of the synaptic and anatomic data, finding largely overlapping distributions (Fig. 10*C*). For reference, this plot annotates the expected ratio from studies of different interneuron types in layers 4 and 5/6 of somatosensory cortex (Cruikshank et al., 2010).

Short-term plasticity of long-range excitation to PV+ and SOM+ neurons

Our measurements of synaptic strength were based on monosynaptic input under recording conditions (TTX, CPP, 4-AP) that monitor synaptic responses to the first stimulus. These measurements might not reflect the relative contribution of the two interneuronal populations to a train of stimuli, which might be more physiological. As PV+ and SOM+ neurons show differences in short-term plasticity of local excitatory inputs (Beierlein et al., 2003), we were interested to test whether later synaptic inputs in a train might alter which interneuron population was more likely to carry feedforward inhibition.

To measure short-term synaptic plasticity, we shifted to expressing a kinetically rapid channelrhodopsin, Chronos (Klapoetke et al., 2014). We stimulated Chronos-GFP+ afferents at 10, 20, and 40 Hz using a 470 nm LED (Fig. 11). Sweeps were averaged and data normalized to the amplitude of the first pulse. For S1 inputs to PV+ neurons, the synaptic inputs were depressing for all frequencies, and most strongly depressing for higher frequencies (Fig. 11*A*, middle and right). Similarly, PO inputs to PV+ neurons were also depressing (Fig. 11*B*). We compared plasticity across synaptic connection types and found that the degree of depression was greater for PO inputs than for S1 for all frequencies tested (Fig. 11*E*), suggesting recovery from short-term depression is slower in PO than in S1 afferents. In contrast to these results in PV+ neurons, SOM+ cells showed some degree of facilitation for both classes of input, although this was not significant for all comparisons. The facilitation was most pronounced for PO inputs to SOM+ neurons (Fig.

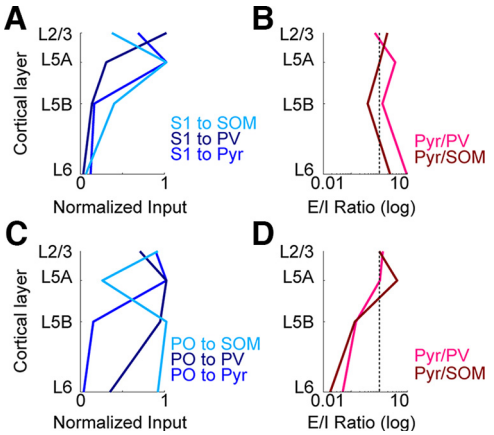

Figure 9. Excitation/inhibition ratio estimated by monosynaptic input mapping. ***A***, Normalized monosynaptic input from S1 to Pyr, PV+, or SOM+ neurons. ***B***, Excitation/inhibition ratio plotted as the ratio of normalized Pyr input in ***A***, divided by either PV (light red) or SOM (dark red). ***C***, Normalized monosynaptic input from PO to Pyr, PV+, or SOM+ neurons. ***D***, Excitation/inhibition ratio plotted as the ratio of normalized Pyr input in ***C***, divided by either PV (light red) or SOM (dark red).

11*C*,*D*). In comparison to input to SOM+ cells, PO inputs were significantly more depressing to PV+ cells at all stimulus frequencies (Fig. 11*F*). This difference was present (at 20 and 40 Hz stimuli) but less pronounced when comparing S1 inputs to PV+ and SOM+ neurons.

These experiments were performed using the same viral vector and recording conditions for both mouse lines, suggesting that the short-term plasticity observed differed between postsynaptic targets and was not due exclusively to an artifact of measuring short-term plasticity with optical methods (Jackman et al., 2014). We do not know whether the same axon might have different release properties depending on its cellular target (Beierlein et al., 2003; Gabernet et al., 2005) or whether different long-range axons from these areas preferentially innervate PV+ and SOM+ neurons.

Discussion

Axon and dendrite overlap determines potential functional connectivity (Peters and Feldman, 1976; Braitenberg and Schuz, 1998). But many excitatory and inhibitory neuron types exist (Tremblay et al., 2016; Tasic et al., 2018), each with potential cell type-specific rules for connectivity (Porter et al., 2000). Here, we show that cortical and thalamic inputs to M1 excite two types of inhibitory interneurons in different and complementary ways. S1 inputs most strongly targeted L2/3 PV+ neurons but SOM+ neurons in middle layers (L5A and L5B). Further, although S1 and PO both targeted pyramidal neurons in L2/3 and L5A with similar connection strength, these pathways targeted PV+ neurons in a different fashion. Thus, cortical and thalamic afferents form highly specific connections in neocortex. The recruitment of feedforward inhibition may not be simply a generic blanket of inhibition, but instead is formed into specific feedforward circuits.

Specific circuits for feedforward inhibition

Motor cortex integrates input from frontal cortical areas (Reep et al., 1990; Rouiller et al., 1993; Dum and Strick, 2002), primary and secondary sensory cortex (Porter et al., 1990; Kaneko et al., 1994a; Hoffer et al., 2003; Chakrabarti and Alloway, 2006; Smith and Alloway, 2013; Suter and Shepherd, 2015), retrosplenial cortex (Yamawaki et al., 2016); and thalamic nuclei (Strick and Sterling, 1974; Deschênes et al., 1998; Kuramoto et al., 2009; Ohno et al., 2012). These inputs activate M1 during voluntary and sensory guided movement, with each targeting excitatory neurons in M1 in a layer-specific manner (Hooks et al., 2013). Different intermingled M1 neurons respond to sensory input or during motor behavior such as whisking, licking, or lever pressing (Armstrong and Drew, 1984; Murray and Keller, 2011; Huber et al., 2012; Harrison and Murphy, 2014; Masamizu et al., 2014; Tanaka et al., 2018), suggesting that individual neurons are parts of different networks, receiving cortical inputs of different strength. We tested whether this pattern is the same for functional synaptic input to interneurons, finding that the laminar pattern of excitation varies with the postsynaptic cell type targeted.

Each excitatory pathway evokes feedforward inhibition to some degree (Isaacson and Scanziani, 2011). This disynaptic inhibition might serve to terminate continuing excitation from the same inputs. Once recruited, local circuit interneurons connect to large numbers of nearby pyramidal neurons (Bock et al., 2011; Fino and Yuste, 2011; Packer and Yuste, 2011). This blanket of inhibition hypothesis proposes that interneurons generally reduce activity nonspecifically, effectively suppressing cortical activity (Fino et al., 2013), although connection strength could be specifically weighted by activity-dependent (Xue et al., 2014) or experience-dependent (Chen et al., 2015) plasticity mechanisms. Our mapping tests the hypothesis of whether the recruitment of feedforward inhibition proceeds by each afferent targeting interneurons nonspecifically or by specifically exciting distinct interneurons. Our results show that cortical and thalamic inputs selectivity activate inhibitory circuitry.

What is the functional relevance of specific feedforward connectivity? If afferents activate selected interneuron subsets, then certain inputs activate some cortical networks while silencing others. For M1, this might activate the appropriate response to sensory stimuli while inhibiting other responses. Pyramidal neurons in different cortical layers project to different (but partially overlapping) targets, including corticocortical, corticostriatal, corticothalamic, and pyramidal tract type projections (Harris and Shepherd, 2015; Callaway et al., 2021). Thus, differences in laminar inhibition may shape the pattern of M1 output to specific targets. S1 activation of L2/3 PV+ neurons might be expected to most strongly silence output of L2/3 pyramids, resulting in reduced feedforward excitation to local L5 pyramidal neurons (Weiler et al., 2008; Hooks et al., 2011) and long-range corticocortical connections (Harris and Shepherd, 2015). Notably, although both S1 and PO pathways excite L5B more weakly than other layers (Mao et al., 2011; Hooks et al., 2013), PO excited both PV+ and SOM+ interneurons in this layer, which might aid in terminating signals associated with inappropriate motor responses. Low excitatory neuron activation coupled with inhibition would increase the signal-to-noise ratio of outgoing motor signals. It is unknown if there is specific targeting to certain pyramidal neuron subtypes. L5B contains two main classes of output neurons, intratelencephalic-type cells projecting to both cortex and striatum, as well as pyramidal-tract-type cells that target striatum, thalamus, brainstem, and spinal cord (Shepherd, 2013; Hooks et al., 2018). Thus, a range of cortical output channels might be suppressed.

In addition to layer-specific differences in connection strength, specific circuits may differ in weight during an incoming train of stimuli. PV inhibition in L2/3 will attenuate with

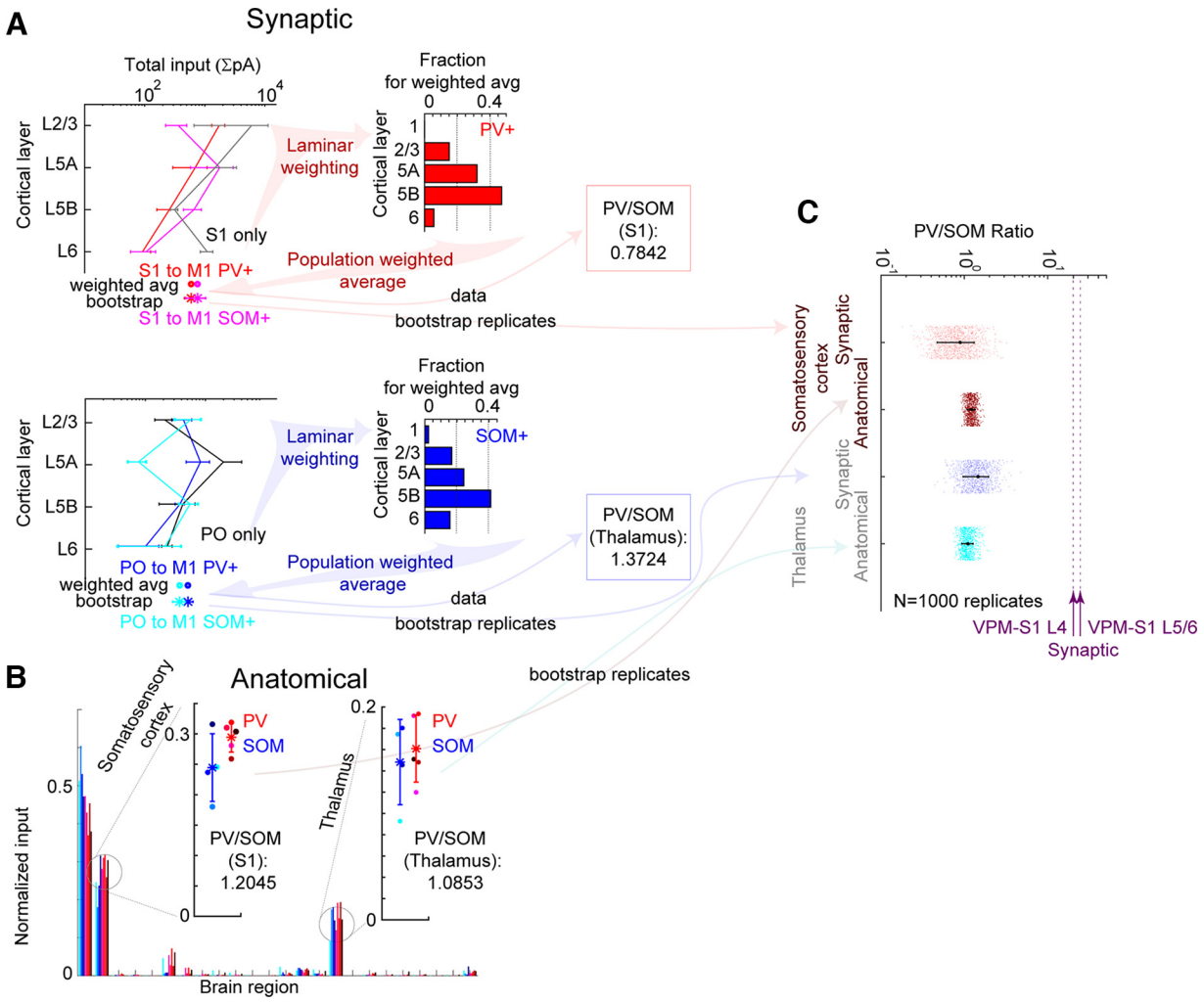

Figure 10. Direct comparison of synaptic and anatomic connectivity. (***A***) Left, absolute synaptic input strength plotted for comparison between S1 inputs to PV+ and SOM+ neurons. Right, the distribution of interneurons per layer (PV+ neurons in the top example). The weighted average input strength is shown below the graph, either as a single point (weighted average) or the mean and SEM from $N = 10{,}000$ replicate (bootstrap) analysis. The ratio of input to PV/SOM is shown for the data in each plot. This ratio can be computed for both S1 (top) and PO (bottom). ***B***, Comparison of anatomic input to PV+ ($N = 5$) and SOM+ ($N = 4$) neurons in M1 from retrograde tracing (after Fig. 1). Insets, Normalized fraction of input from each case. The ratio of input to PV/SOM is shown for each plot. ***C***, Comparison of PV/SOM input for synaptic inputs (from S1, red; from PO, blue) and for anatomic tracing (in S1, green; in thalamus, gray). PV/SOM comparison for thalamus (VPM) to S1 layers 4 and 5/6 (Cruikshank et al., 2010) added for reference. The data were resampled for $N = 1000$ replicates to compare.

time, whereas SOM inhibition in L5A may be facilitated. This interpretation requires validation as SOM+ neurons may inhibit PV+ cells, helping to disinhibit cortex (Pfeffer et al., 2013) and complicating the picture.

Organization of long-range input to SOM+ interneurons differs across cortical areas

Previous work shows that SOM+ neurons in L4 of sensory areas received weaker input than neighboring pyramidal neurons and PV+ neurons (Bruno and Simons, 2002; Cruikshank et al., 2007; 2010). This thalamocortical preference for PV+ over SOM+ neurons in somatosensory cortex extends to L2/3 (Naskar et al., 2021). Thalamic input to SOM+ does exist in sensory areas, although it may be developmentally downregulated at ages younger than those studied here (Marques-Smith et al., 2016; Tuncdemir et al., 2016). Thus, we were surprised to find many layers in M1 where SOM+ cells received comparable inputs to PV+ cells (Fig. 8) in monosynaptic input mapping (Porter et al., 2001). Comparisons are challenging because of limitations of normalizing input strength across different injections in different animals (Petreanu et al., 2009). But the mean thalamic input strength to SOM+ interneurons was marginally higher than that to PV+ neurons except for L5A (Fig. 8*H*, middle right). However, there is considerable variability among cells (Fig. 8*G*). Similarly, corticocortical input from S1 was higher to SOM+ neurons in L5A and L5B (Fig. 8*H*, top right). This collectively suggests that there is no uniform rule that thalamic input will be selective for PV+ neurons across all cortical areas and layers.

In addition to input strength, input from S1 and PO will not occur in isolation but as part of trains of action potentials, especially should thalamus fire in burst mode (Steriade et al., 1993; Sherman, 2001). In the case of PO, short-term depression of input to PV+ neurons is the strongest short-term plasticity we observed (Fig. 11). In contrast, these inputs were facilitating to SOM+ neurons. This suggests that as rapidly as the second or third pulse in a train, the recruitment of feedforward inhibition could shift from PV+ to SOM+ neurons (Tan et al., 2008). The difference in short-term plasticity to SOM+ and PV+ neurons is not as large for S1 afferents as for PO inputs, although the

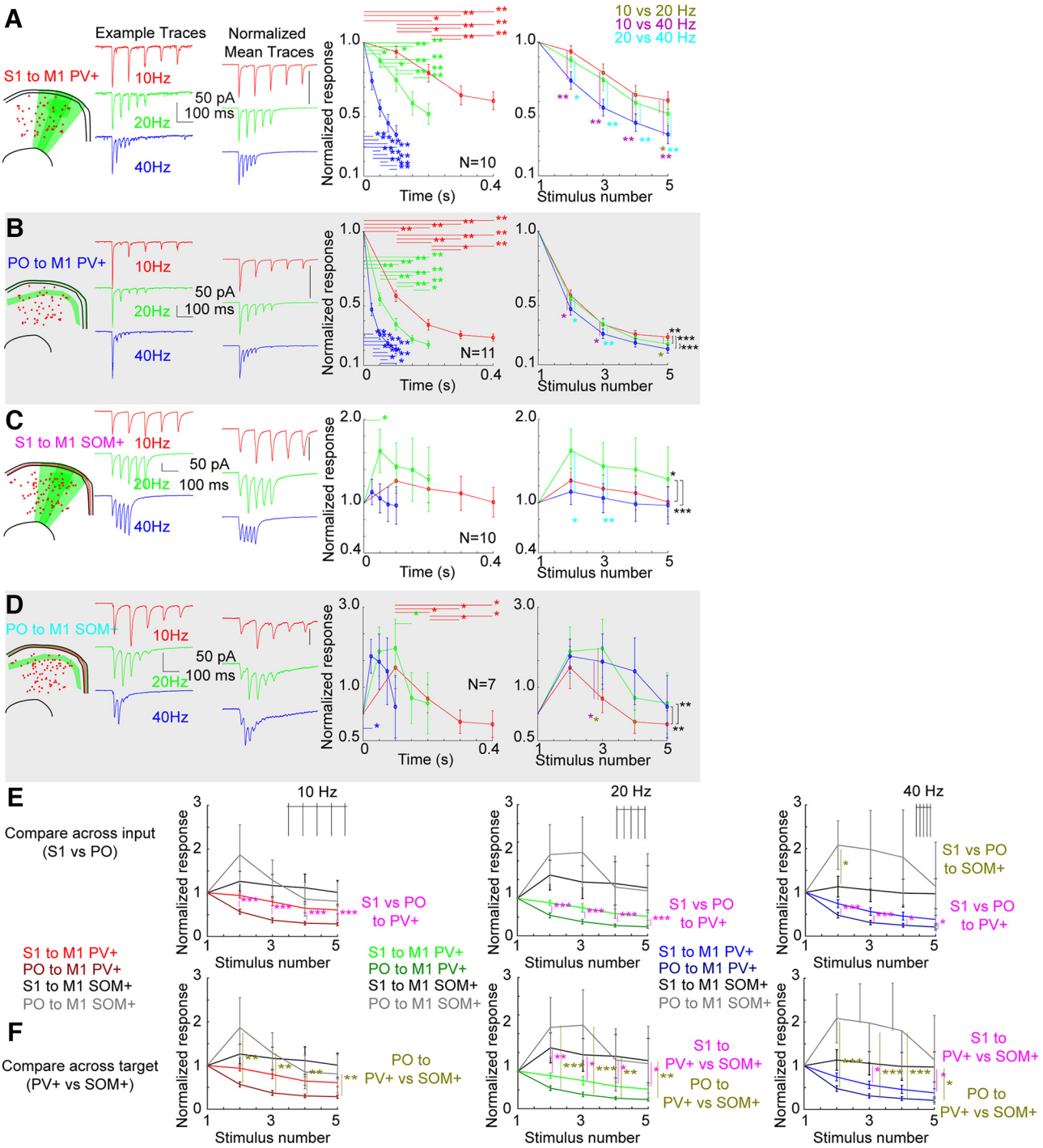

Figure 11. Short-term plasticity at long-range inputs to interneurons of mouse motor cortex. ***A***, Short-term plasticity of S1 input to PV+ neurons. Left, Example traces showing PV+ neuron response to S1 stimulation at 10 Hz (red), 20 Hz (green), and 40 Hz (blue) stimulation of Chronos-GFP+ S1 axons. Calibration, 50 pA, 100 ms. Middle, Average normalized traces for the same stimulus frequencies. Calibration, 1.0 (normalized) Right, Summary graphs showing normalized responses for 10 Hz, 20 Hz, and 40 Hz. Graphs are plotted based on time of the pulses (right) or the stimulus number (far right). Statistical differences noted for each stimulus frequency in the appropriate color for differences in amplitude across stimulus number (related-samples Wilcoxon signed-rank test) or for amplitude differences at the end of the train across stimulus frequency (related-samples Wilcoxon signed-rank test, vertical bars on right). ***B***, Short-term plasticity of PO input to PV+ neurons, plotted as in ***A***. ***C***, Short-term plasticity of S1 input to SOM+ neurons, plotted as in ***A***. ***D***, Short-term plasticity of PO input to SOM+ neurons, plotted as in ***A***. ***E, F***, Comparison of facilitation and depression across cell types at 10 Hz (top), 20 Hz (middle), and 40 Hz (bottom). ***E***, This row contrasts cortical (S1, purple) versus thalamic (PO, gold) inputs to a given cell type. ***F***, This row compares cortical inputs (S1) across cell types (PV+ and SOM+, purple). Thalamic (PO) comparison shown in gold. Assessed by independent samples Mann–Whitney *U* test. $^{*}p < 0.05$, $^{**}p < 0.01$, $^{***}p < 0.001$.

general pattern is the same. If inhibition from SOM+ neurons is facilitating in M1 (Beierlein et al., 2003), then this would serve to further shift the balance of disynaptic feedforward inhibition from PV+ to SOM+ neurons, giving SOM+ neurons the potential to play a role in regulating excitability and plasticity (Chen et al., 2015).

Comparison of anatomic and functional methods for mapping microcircuitry

The emergence of techniques for recording, imaging, and reconstructing the whole brain present a great deal of data to deepen our understanding of how neocortical areas are connected and

function at large scales. Imaging projections from defined neurons (Oh et al., 2014; Zingg et al., 2014; Jeong et al., 2016) to label long-range targets or retrograde viral methods to label presynaptic inputs (Wickersham et al., 2007a; Luo et al., 2018) offer hope for efficiently identifying connectivity in whole-brains images aligned to standardized coordinate systems (Kuan et al., 2015; Hooks et al., 2018; Eastwood et al., 2019). Thus, monosynaptic tracing with rabies virus has substantial appeal. A comparison across large-scale recording methods (high channel count probes or calcium imaging), synaptic connectivity, and anatomic projections would help clarify how neural connectivity contributes to brain function.

Here, we directly compared synaptic input and retrograde anatomic tracing of presynaptic input to M1 interneurons. Based on prior work, we hypothesized that thalamocortical input would favor PV+ interneurons. In S1, thalamic inputs to fast-spiking (presumed PV+) neurons were more likely to be connected (Bruno and Simons, 2002) and were vastly stronger by EPSC amplitude, as much as 10–20× in L4 and L5/6 (Fig. 6; Cruikshank et al., 2010) as well as later 2/3 (Fig. 2; Naskar et al., 2021). In M1, in contrast, both synaptic connectivity mapping experiments and retrograde viral tracing data showed strong thalamocortical connections to PV+ and SOM+ neurons in M1 (Figs. 1, 6–9). Indeed, input to PV+ neurons was only ~10–30% stronger than that to SOM+ neurons (Fig. 10). This difference was not significant in the anatomy data, although nonsignificant trends (Fig. 1) were present in three thalamic nuclei not assessed functionally (VM, PC, and PF). Thus, both measures of anatomic and functional connectivity were consistent in demonstrating distinct thalamocortical connectivity rules for primary motor cortex compared with sensory cortex. Similarly, our measures of corticocortical input to SOM+ neurons were comparable between anatomic and functional methods (Fig. 10), although the functional method showed a slight preference for SOM+ neurons (because of stronger input to the more numerous interneuron population in L5A and L5B), whereas the anatomic method showed a nonsignificant trend for larger S1 input to PV+ neurons (Fig. 1).

There are some limitations to the comparison. With anatomic methods, it was not possible to label SOM+ or PV+ interneurons in specific layers and show differences in connectivity as was the case in functional mapping experiments. Thus, variability in anatomic cases is reduced because results from multiple individual starter cells are summed in each experiment, whereas whole-cell recording emphasizes the variability between different cells, shown as individual input vectors (Figs. 4*B*–7*B*). Furthermore, quantifying differences in synaptic strength is not the same as counting presynaptic neurons. The relationship between synaptic strength, number of connection sites, and rabies spread is not perfectly understood. Although we hypothesize that stronger synaptic connections result in more points of contact between corticocortical or thalamocortical axons and rabies-infected starter cells, there are no control experiments to show this increases rabies labeled neurons. Furthermore, although we can quantify synaptic strength to PV+ or SOM+ neurons from S1 or PO inputs in a given layer, it is not certain that deriving a single value for connection strength for the whole population is the strongest means to make such a comparison.

How reliable is retrograde labeling for anatomically assessing connectivity? The data presented here suggest anatomic and functional methods can predict similar connectivity. First, the retrograde tracing data provides strong support for retrograde tracing as an effective measure of area-to-area connectivity. Tracing from starter cells in each cortical area specifically labeled a pattern of both cortical areas and thalamic nuclei unique to that cortical area and reproducibly across replicates (Fig. 2*B*–*E*; individual replicates are plotted in Fig. 10*B* as well). For example, M2 gets input from limbic areas, whereas M1 and S1 do not. Furthermore, even small brain areas, such as individual thalamic nuclei, have distinct patterns of label for each of the three cortical areas studies. However, because the specific thalamic labeling was almost identical for input to PV+ and SOM+ interneurons for the regions that we studied, evidence that retrograde tracing varies strongly with postsynaptic target would be better tested in cell types with vastly different connectivity, especially where afferents avoid innervating one cell type while connecting strongly to another intermingled type.

Conclusion

Overall, these results quantify how different cortical and thalamic inputs excite specific interneurons in a layer and cell type-specific pattern. Cortical and thalamic input excites M1 PV+ neurons in different, complementary layers, in contrast to its targeting of excitatory cells. In contrast to sensory cortex, thalamic input excites SOM+ interneurons with similar strength to PV+ interneurons.

References

Anderson CT, Sheets PL, Kiritani T, Shepherd GM (2010) Sublayer-specific microcircuits of corticospinal and corticostriatal neurons in motor cortex. Nat PM 13:739–744.

Armstrong DM, Drew T (1984) Topographical localization in the motor cortex of the cat for somatic afferent responses and evoked movements. J Physiol 350:33–54.

Asanuma H (1981) Functional role of sensory inputs to the motor cortex. Prog Neurobiol 16:241–262.

Atasoy D, Aponte Y, Su HH, Sternson SM (2008) A FLEX switch targets Channelrhodopsin-2 to multiple cell types for imaging and long-range circuit mapping. J Neurosci 28:7025–7030.

Beierlein M, Gibson JR, Connors BW (2003) Two dynamically distinct inhibitory networks in layer 4 of the neocortex. J Neurophysiol 90:2987–3000.

Benjamini Y, Heller R, Yekutieli D (2009) Selective inference in complex research. Philos Trans A Math Phys Eng Sci 367:4255–4271.

Bock DD, Lee WC, Kerlin AM, Andermann ML, Hood G, Wetzel AW, Yurgenson S, Soucy ER, Kim HS, Reid RC (2011) Network anatomy and *in vivo* physiology of visual cortical neurons. Nature 471:177–182.

Braitenberg VB, Schuz A (1998) Cortex: statistics and geometry of neuronal connectivity. Berlin: Springer.

Bruno RM, Simons DJ (2002) Feedforward mechanisms of excitatory and inhibitory cortical receptive fields. J Neurosci 22:10966–10975.

Callaway EM, Luo L (2015) Monosynaptic circuit tracing with glycoprotein-deleted rabies viruses. J Neurosci 35:8979–8985.

Callaway EM, et al. (2021) A multimodal cell census and atlas of the mammalian primary motor cortex. Nature 598:86–102.

Cauli B, Audinat E, Lambolez B, Angulo MC, Ropert N, Tsuzuki K, Hestrin S, Rossier J (1997) Molecular and physiological diversity of cortical nonpyramidal cells. J Neurosci 17:3894–3906.

Chakrabarti S, Alloway KD (2006) Differential origin of projections from SI barrel cortex to the whisker representations in SII and MI. J Comp Neurol 498:624–636.

Chen SX, Kim AN, Peters AJ, Komiyama T (2015) Subtype-specific plasticity of inhibitory circuits in motor cortex during motor learning. Nat Neurosci 18:1109–1115.

Cruikshank SJ, Lewis TJ, Connors BW (2007) Synaptic basis for intense thalamocortical activation of feedforward inhibitory cells in neocortex. Nat Neurosci 10:462–468.

Cruikshank SJ, Urabe H, Nurmikko AV, Connors BW (2010) Pathway-specific feedforward circuits between thalamus and neocortex revealed by selective optical stimulation of axons. Neuron 65:230–245.

Deschênes M, Veinante P, Zhang ZW (1998) The organization of corticothalamic projections: reciprocity versus parity. Brain Res Brain Res Rev 28:286–308.

Dittrich L, Heiss JE, Warrier DR, Perez XA, Quik M, Kilduff TS (2012) Cortical nNOS neurons co-express the NK1 receptor and are depolarized by Substance P in multiple mammalian species. Front Neural Circuits 6:31.

Donoghue JP, Wise SP (1982) The motor cortex of the rat: cytoarchitecture and microstimulation mapping. J Comp Neurol 212:76–88.

Dum RP, Strick PL (2002) Motor areas in the frontal lobe of the primate. Physiol Behav 77:677–682.

Eastwood BS, Hooks BM, Paletzki RF, O'Connor NJ, Glaser JR, Gerfen CR (2019) Whole mouse brain reconstruction and registration to a reference atlas with standard histochemical processing of coronal sections. J Comp Neurol 527:2170–2178.

Ferezou I, Haiss F, Gentet LJ, Aronoff R, Weber B, Petersen CC (2007) Spatiotemporal dynamics of cortical sensorimotor integration in behaving mice. Neuron 56:907–923.

Fino E, Yuste R (2011) Dense inhibitory connectivity in neocortex. Neuron 69:1188–1203.

Fino E, Packer AM, Yuste R (2013) The logic of inhibitory connectivity in the neocortex. Neuroscientist 19:228–237.

Gabernet L, Jadhav SP, Feldman DE, Carandini M, Scanziani M (2005) Somatosensory integration controlled by dynamic thalamocortical feedforward inhibition. Neuron 48:315–327.

Gibson JR, Beierlein M, Connors BW (1999) Two networks of electrically coupled inhibitory neurons in neocortex. Nature 402:75–79.

Harris JA, et al. (2019) Hierarchical organization of cortical and thalamic connectivity. Nature 575:195–202.

Harris KD, Shepherd GM (2015) The neocortical circuit: themes and variations. Nat Neurosci 18:170–181.

Harrison TC, Murphy TH (2014) Motor maps and the cortical control of movement. Curr Opin Neurobiol 24:88–94.

Hatsopoulos NG, Suminski AJ (2011) Sensing with the motor cortex. Neuron 72:477–487.

Hill DN, Curtis JC, Moore JD, Kleinfeld D (2011) Primary motor cortex reports efferent control of vibrissa motion on multiple timescales. Neuron 72:344–356.

Hippenmeyer S, Vrieseling E, Sigrist M, Portmann T, Laengle C, Ladle DR, Arber S (2005) A developmental switch in the response of DRG neurons to ETS transcription factor signaling. PLoS Biol 3:e159.

Hirsch JA, Martinez LM, Pillai C, Alonso JM, Wang Q, Sommer FT (2003) Functionally distinct inhibitory neurons at the first stage of visual cortical processing. Nat Neurosci 6:1300–1308.

Hoffer ZS, Hoover JE, Alloway KD (2003) Sensorimotor corticocortical projections from rat barrel cortex have an anisotropic organization that facilitates integration of inputs from whiskers in the same row. J Comp Neurol 466:525–544.

Hooks BM (2017) Sensorimotor convergence in circuitry of the motor cortex. Neuroscientist 23:251–263.

Hooks BM, Hires SA, Zhang YX, Huber D, Petreanu L, Svoboda K, Shepherd GM (2011) Laminar analysis of excitatory local circuits in vibrissal motor and sensory cortical areas. PLoS Biol 9:e1000572.

Hooks BM, Mao T, Gutnisky DA, Yamawaki N, Svoboda K, Shepherd GM (2013) Organization of cortical and thalamic input to pyramidal neurons in mouse motor cortex. J Neurosci 33:748–760.

Hooks BM, Lin JY, Guo C, Svoboda K (2015) Dual-channel circuit mapping reveals sensorimotor convergence in the primary motor cortex. J Neurosci 35:4418–4426.

Hooks BM, Papale AE, Paletzki RF, Feroze MW, Eastwood BS, Couey JJ, Winnubst J, Chandrashekar J, Gerfen CR (2018) Topographic precision in sensory and motor corticostriatal projections varies across cell type and cortical area. Nat Commun 9:3549.

Huang H, Kuzirian MS, Cai X, Snyder LM, Cohen J, Kaplan DH, Ross SE (2016) Generation of a NK1R-CreER knockin mouse strain to study cells involved in Neurokinin 1 receptor signaling. Genesis 54:593–601.

Huber D, Gutnisky DA, Peron S, O'Connor DH, Wiegert JS, Tian L, Oertner TG, Looger LL, Svoboda K (2012) Multiple dynamic representations in the motor cortex during sensorimotor learning. Nature 484:473–478.

Isaacson JS, Scanziani M (2011) How inhibition shapes cortical activity. Neuron 72:231–243.

Jackman SL, Beneduce BM, Drew IR, Regehr WG (2014) Achieving high-frequency optical control of synaptic transmission. J Neurosci 34:7704–7714.

Jeong M, Kim Y, Kim J, Ferrante DD, Mitra PP, Osten P, Kim D (2016) Comparative three-dimensional connectome map of motor cortical projections in the mouse brain. Sci Rep 6:20072.

Kaneko T, Caria MA, Asanuma H (1994a) Information processing within the motor cortex. I. Responses of morphologically identified motor cortical cells to stimulation of the somatosensory cortex. J Comp Neurol 345:161–171.

Kaneko T, Caria MA, Asanuma H (1994b) Information processing within the motor cortex. II. Intracortical connections between neurons receiving somatosensory cortical input and motor output neurons of the cortex. J Comp Neurol 345:172–184.

Kätzel D, Zemelman BV, Buetfering C, Wölfel M, Miesenböck G (2011) The columnar and laminar organization of inhibitory connections to neocortical excitatory cells. Nat Neurosci 14:100–107.

Kawaguchi Y, Kubota Y (1997) GABAergic cell subtypes and their synaptic connections in rat frontal cortex. Cereb Cortex 7:476–486.

Keller A, White EL (1987) Synaptic organization of GABAergic neurons in the mouse SmI cortex. J Comp Neurol 262:1–12.

Kinnischtzke AK, Simons DJ, Fanselow EE (2014) Motor cortex broadly engages excitatory and inhibitory neurons in somatosensory barrel cortex. Cereb Cortex 24:2237–2248.

Kiritani T, Wickersham IR, Seung HS, Shepherd GM (2012) Hierarchical connectivity and connection-specific dynamics in the corticospinal-corticostriatal microcircuit in mouse motor cortex. J Neurosci 32:4992–5001.

Klapoetke NC, et al. (2014) Independent optical excitation of distinct neural populations. Nat Methods 11:338–346.

Kuan L, Li Y, Lau C, Feng D, Bernard A, Sunkin SM, Zeng H, Dang C, Hawrylycz M, Ng L (2015) Neuroinformatics of the Allen Mouse Brain Connectivity Atlas. Methods 73:4–17.

Kubota Y (2014) Untangling GABAergic wiring in the cortical microcircuit. Curr Opin Neurobiol 26:7–14.

Kubota Y, Shigematsu N, Karube F, Sekigawa A, Kato S, Yamaguchi N, Hirai Y, Morishima M, Kawaguchi Y (2011) Selective coexpression of multiple chemical markers defines discrete populations of neocortical GABAergic neurons. Cereb Cortex 21:1803–1817.

Kuramoto E, Furuta T, Nakamura KC, Unzai T, Hioki H, Kaneko T (2009) Two types of thalamocortical projections from the motor thalamic nuclei of the rat: a single neuron-tracing study using viral vectors. Cereb Cortex 19:2065–2077.

Kuramoto E, Ohno S, Furuta T, Unzai T, Tanaka YR, Hioki H, Kaneko T (2015) Ventral medial nucleus neurons send thalamocortical afferents more widely and more preferentially to layer 1 than neurons of the ventral anterior-ventral lateral nuclear complex in the rat. Cereb Cortex 25:221–235.

Lee S, Hjerling-Leffler J, Zagha E, Fishell G, Rudy B (2010) The largest group of superficial neocortical GABAergic interneurons expresses ionotropic serotonin receptors. J Neurosci 30:16796–16808.

Luo L, Callaway EM, Svoboda K (2018) Genetic dissection of neural circuits: a decade of progress. Neuron 98:865.

Ma Y, Hu H, Berrebi AS, Mathers PH, Agmon A (2006) Distinct subtypes of somatostatin-containing neocortical interneurons revealed in transgenic mice. J Neurosci 26:5069–5082.

Madisen L, Zwingman TA, Sunkin SM, Oh SW, Zariwala HA, Gu H, Ng LL, Palmiter RD, Hawrylycz MJ, Jones AR, Lein ES, Zeng H (2010) A robust and high-throughput Cre reporting and characterization system for the whole mouse brain. Nat Neurosci 13:133–140.

Mao T, Kusefoglu D, Hooks BM, Huber D, Petreanu L, Svoboda K (2011) Long-range neuronal circuits underlying the interaction between sensory and motor cortex. Neuron 72:111–123.

Marques-Smith A, Lyngholm D, Kaufmann AK, Stacey JA, Hoerder-Suabedissen A, Becker EB, Wilson MC, Molnár Z, Butt SJ (2016) A transient translaminar GABAergic interneuron circuit connects thalamocortical recipient layers in neonatal somatosensory cortex. Neuron 89:536–549.

Masamizu Y, Tanaka YR, Tanaka YH, Hira R, Ohkubo F, Kitamura K, Isomura Y, Okada T, Matsuzaki M (2014) Two distinct layer-specific dynamics of cortical ensembles during learning of a motor task. Nat Neurosci 17:987–994.

Muñoz-Castañeda R, et al. (2021) Cellular anatomy of the mouse primary motor cortex. Nature 598:159–166.

Murray PD, Keller A (2011) Somatosensory response properties of excitatory and inhibitory neurons in rat motor cortex. J Neurophysiol 106:1355–1362.

Naka A, Veit J, Shababo B, Chance RK, Risso D, Stafford D, Snyder B, Egladyous A, Chu D, Sridharan S, Mossing DP, Paninski L, Ngai J, Adesnik H (2019) Complementary networks of cortical somatostatin interneurons enforce layer specific control. Elife 8:e43696.

Naskar S, Qi J, Pereira F, Gerfen CR, Lee S (2021) Cell-type-specific recruitment of GABAergic interneurons in the primary somatosensory cortex by long-range inputs. Cell Rep 34:108774.

Oh SW, et al. (2014) A mesoscale connectome of the mouse brain. Nature 508:207–214.

Ohno S, Kuramoto E, Furuta T, Hioki H, Tanaka YR, Fujiyama F, Sonomura T, Uemura M, Sugiyama K, Kaneko T (2012) A morphological analysis of thalamocortical axon fibers of rat posterior thalamic nuclei: a single neuron tracing study with viral vectors. Cereb Cortex 22:2840–2857.

Packer AM, Yuste R (2011) Dense, unspecific connectivity of neocortical parvalbumin-positive interneurons: a canonical microcircuit for inhibition? J Neurosci 31:13260–13271.

Peters A, Feldman ML (1976) The projection of the lateral geniculate nucleus to area 17 of the rat cerebral cortex. I. General description. J Neurocytol 5:63–84.

Petreanu L, Huber D, Sobczyk A, Svoboda K (2007) Channelrhodopsin-2-assisted circuit mapping of long-range callosal projections. Nat Neurosci 10:663–668.

Petreanu L, Mao T, Sternson SM, Svoboda K (2009) The subcellular organization of neocortical excitatory connections. Nature 457:1142–1145.

Pfeffer CK, Xue M, He M, Huang ZJ, Scanziani M (2013) Inhibition of inhibition in visual cortex: the logic of connections between molecularly distinct interneurons. Nat Neurosci 16:1068–1076.

Porter JT, Johnson CK, Agmon A (2001) Diverse types of interneurons generate thalamus-evoked feedforward inhibition in the mouse barrel cortex. J Neurosci 21:2699–2710.

Porter LL, White EL (1983) Afferent and efferent pathways of the vibrissal region of primary motor cortex in the mouse. J Comp Neurol 214:279–289.

Porter LL, Sakamoto T, Asanuma H (1990) Morphological and physiological identification of neurons in the cat motor cortex which receive direct input from the somatic sensory cortex. Exp Brain Res 80:209–212.

Porter LL, Matin D, Keller A (2000) Characteristics of GABAergic neurons and their synaptic relationships with intrinsic axons in the cat motor cortex. Somatosens Mot Res 17:67–80.

Prönneke A, Scheuer B, Wagener RJ, Möck M, Witte M, Staiger JF (2015) Characterizing VIP neurons in the barrel cortex of VIPcre/tdTomato mice reveals layer-specific differences. Cereb Cortex 25:4854–4868.

Reardon TR, Murray AJ, Turi GF, Wirblich C, Croce KR, Schnell MJ, Jessell TM, Losonczy A (2016) Rabies virus CVS-N2c(ΔG) strain enhances retrograde synaptic transfer and neuronal viability. Neuron 89:711–724.

Reep RL, Goodwin GS, Corwin JV (1990) Topographic organization in the corticocortical connections of medial agranular cortex in rats. J Comp Neurol 294:262–280.

Rocco-Donovan M, Ramos RL, Giraldo S, Brumberg JC (2011) Characteristics of synaptic connections between rodent primary somatosensory and motor cortices. Somatosens Mot Res 28:63–72.

Rouiller EM, Moret V, Liang F (1993) Comparison of the connectional properties of the two forelimb areas of the rat sensorimotor cortex: support for the presence of a premotor or supplementary motor cortical area. Somatosens Mot Res 10:269–289.

Scala F, Kobak D, Bernabucci M, Bernaerts Y, Cadwell CR, Castro JR, Hartmanis L, Jiang X, Laturnus S, Miranda E, Mulherkar S, Tan ZH, Yao Z, Zeng H, Sandberg R, Berens P, Tolias AS (2021) Phenotypic variation of transcriptomic cell types in mouse motor cortex. Nature 598:144–150.

Shepherd GM (2013) Corticostriatal connectivity and its role in disease. Nat Rev Neurosci 14:278–291.

Shepherd GM, Pologruto TA, Svoboda K (2003) Circuit analysis of experience-dependent plasticity in the developing rat barrel cortex. Neuron 38:277–289.

Sherman SM (2001) Tonic and burst firing: dual modes of thalamocortical relay. Trends Neurosci 24:122–126.

Smith JB, Alloway KD (2013) Rat whisker motor cortex is subdivided into sensory-input and motor-output areas. Front Neural Circuits 7:4.

Steriade M, McCormick DA, Sejnowski TJ (1993) Thalamocortical oscillations in the sleeping and aroused brain. Science 262:679–685.

Strick PL, Sterling P (1974) Synaptic termination of afferents from the ventrolateral nucleus of the thalamus in the cat motor cortex. A light and electron microscopy study. J Comp Neurol 153:77–106.

Suter BA, Shepherd GM (2015) Reciprocal interareal connections to corticospinal neurons in mouse M1 and S2. J Neurosci 35:2959–2974.

Suter BA, O'Connor T, Iyer V, Petreanu LT, Hooks BT, Kiritani T, Svoboda K, Sheperd GMG (2010) Ephus: multipurpose data acquisition software for neuroscience experiments. Front Neural Circuits Neurosci 4:100.

Tan Z, Hu H, Huang ZJ, Agmon A (2008) Robust but delayed thalamocortical activation of dendritic-targeting inhibitory interneurons. Proc Natl Acad Sci U S A 105:2187–2192.

Tanaka YH, Tanaka YR, Kondo M, Terada SI, Kawaguchi Y, Matsuzaki M (2018) Thalamocortical axonal activity in motor cortex exhibits layer-specific dynamics during motor learning. Neuron 100:244–258.e12.

Taniguchi H, He M, Wu P, Kim S, Paik R, Sugino K, Kvitsiani D, Kvitsani D, Fu Y, Lu J, Lin Y, Miyoshi G, Shima Y, Fishell G, Nelson SB, Huang ZJ (2011) A resource of Cre driver lines for genetic targeting of GABAergic neurons in cerebral cortex. Neuron 71:995–1013.

Tasic B, et al. (2018) Shared and distinct transcriptomic cell types across neocortical areas. Nature 563:72–78.

Tremblay R, Lee S, Rudy B (2016) GABAergic interneurons in the neocortex: from cellular properties to circuits. Neuron 91:260–292.

Tuncdemir SN, Wamsley B, Stam FJ, Osakada F, Goulding M, Callaway EM, Rudy B, Fishell G (2016) Early somatostatin interneuron connectivity mediates the maturation of deep layer cortical circuits. Neuron 89:521–535.

Wang Y, Toledo-Rodriguez M, Gupta A, Wu C, Silberberg G, Luo J, Markram H (2004) Anatomical, physiological and molecular properties of Martinotti cells in the somatosensory cortex of the juvenile rat. J Physiol 561:65–90.

Weiler N, Wood L, Yu J, Solla SA, Shepherd GM (2008) Top-down laminar organization of the excitatory network in motor cortex. Nat Neurosci 11:360–366.

White EL (1979) Thalamocortical synaptic relations: a review with emphasis on the projections of specific thalamic nuclei to the primary sensory areas of the neocortex. Brain Res 180:275–311.

Wickersham IR, Finke S, Conzelmann KK, Callaway EM (2007a) Retrograde neuronal tracing with a deletion-mutant rabies virus. Nat Methods 4:47–49.

Wickersham IR, Lyon DC, Barnard RJ, Mori T, Finke S, Conzelmann KK, Young JA, Callaway EM (2007b) Monosynaptic restriction of transsynaptic tracing from single, genetically targeted neurons. Neuron 53:639–647.

Xue M, Atallah BV, Scanziani M (2014) Equalizing excitation-inhibition ratios across visual cortical neurons. Nature 511:596–600.

Yamawaki N, Radulovic J, Shepherd GM (2016) A corticocortical circuit directly links retrosplenial cortex to M2 in the mouse. J Neurosci 36:9365–9374.

Zeisel A, Muñoz-Manchado AB, Codeluppi S, Lönnerberg P, La Manno G, Juréus A, Marques S, Munguba H, He L, Betsholtz C, Rolny C, Castelo-Branco G, Hjerling-Leffler J, Linnarsson S (2015) Brain structure. Cell types in the mouse cortex and hippocampus revealed by single-cell RNA-seq. Science 347:1138–1142.

Zingg B, Hintiryan H, Gou L, Song MY, Bay M, Bienkowski MS, Foster NN, Yamashita S, Bowman I, Toga AW, Dong HW (2014) Neural networks of the mouse neocortex. Cell 156:1096–1111.